OPEN ACCESS



Multi-scale Physical Properties of NGC 6334 as Revealed by Local Relative Orientations between Magnetic Fields, Density Gradients, Velocity Gradients, and Gravity

Junhao Liu (刘峻豪) ¹ ¹ ¹ Qizhou Zhang ² ¹ ¹ Patrick M. Koch ³ ¹ Patrick M. A'ohōkū Place, University Park, Hilo, HI 96720, USA; liujunhao42@outlook.com, j.liu@eaobservatory.org ² Patrick M. A'ohōkū Place, University Park, Hilo, HI 96720, USA; liujunhao42@outlook.com, j.liu@eaobservatory.org ² Patrick M. A'ohōkū Place, University Park, Hilo, HI 96720, USA; liujunhao42@outlook.com, j.liu@eaobservatory.org ² Patrick M. A'ohōkū Place, University Park, Hilo, HI 96720, USA; liujunhao42@outlook.com, j.liu@eaobservatory.org ² Patrick M. Otalan, A'ohōkū Place, University Park, Hilo, HI 96720, USA; liujunhao42@outlook.com, j.liu@eaobservatory.org ² Patrick M. Otalan, A'ohōkū Place, University, No. 70, Lien-Hai Road, Kaohsiung City 80424, Taiwan, People's Republic of China ⁴ Physics Department, National Sun Yat-Sen University of Virginia, Charlottesville, VA 22904-4325, USA ⁶ Max Planck Institute for Astronomy, Konigstuhl 17, D-69117 Heidelberg, Germany ⁷ Institut de Ciencies de l'Espai (ICE, CSIC), Can Magrans s/n, E-08193 Cerdanyola del Vallès, Catalonia, Spain ⁸ Institut d'Estudis Espacials de de Catalunya (IEEC), E-08034 Barcelona, Catalonia, Spain ⁹ National Radio Astronomy Observatory, P.O. Box O, Socorro, NM 87801, USA ¹⁰ Institute of Astronomy and Department of Physics, National Tsing Hua University, Hsinchu 30013, Taiwan, Republic of China Patrick Modern Astronomy and Astrophysics (Nanjing University), Ministry of Education, Nanjing 210023, Jiangsu, People's Republic of China Received 2022 October 31; revised 2023 January 8; accepted 2023 January 21; published 2023 March 16

Abstract

We present ALMA dust polarization and molecular line observations toward four clumps (I(N), I, IV, and V) in the massive star-forming region NGC 6334. In conjunction with large-scale dust polarization and molecular line data from JCMT, Planck, and NANTEN2, we make a synergistic analysis of relative orientations between magnetic fields (θ_B) , column density gradients (θ_{NG}) , local gravity (θ_{LG}) , and velocity gradients (θ_{VG}) to investigate the multi-scale (from ~30 to 0.003 pc) physical properties in NGC 6334. We find that the relative orientation between $\theta_{\rm B}$ and $\theta_{\rm NG}$ changes from statistically more perpendicular to parallel as column density $(N_{\rm H_2})$ increases, which is a signature of trans-to-sub-Alfvénic turbulence at complex/cloud scales as revealed by previous numerical studies. Because θ_{NG} and θ_{LG} are preferentially aligned within the NGC 6334 cloud, we suggest that the more parallel alignment between θ_B and θ_{NG} at higher N_{H_2} is because the magnetic field line is dragged by gravity. At even higher $N_{\rm H_2}$, the angle between $\theta_{\rm B}$ and $\theta_{\rm NG}$ or $\theta_{\rm LG}$ transits back to having no preferred orientation, or statistically slightly more perpendicular, suggesting that the magnetic field structure is impacted by star formation activities. A statistically more perpendicular alignment is found between $\theta_{\rm B}$ and $\theta_{\rm VG}$ throughout our studied $N_{\rm H}$, range, which indicates a trans-to-sub-Alfvénic state at small scales as well, and this signifies that magnetic field has an important role in the star formation process in NGC 6334. The normalized mass-to-flux ratio derived from the polarizationintensity gradient (KTH) method increases with $N_{\rm H_2}$, but the KTH method may fail at high $N_{\rm H_2}$ due to the impact of star formation feedback.

Unified Astronomy Thesaurus concepts: Polarimetry (1278); Magnetic fields (994); Star formation (1569); Molecular clouds (1072); Interstellar medium (847)

1. Introduction

Turbulence and magnetic fields are the two major forces that compete with gravity within self-gravitating molecular clouds. The balance among these forces controls the star formation process (McKee & Ostriker 2007). The role of magnetic fields in star formation is less understood than turbulence, due to there being relatively fewer observations. Understanding the interactions between magnetic fields and the other two forces has been a key topic in the study of star formation (Crutcher 2012).

Assuming that the shortest axis of a fraction of irregular dust grains is aligned with the magnetic field, the plane-of-sky (POS) magnetic field orientation can be traced by rotating the observed position angle of linearly polarized dust emission by 90° (Davis & Greenstein 1949; Lazarian 2007; Lazarian & Hoang 2007;

Original content from this work may be used under the terms of the Creative Commons Attribution 4.0 licence. Any further distribution of this work must maintain attribution to the author(s) and the title of the work, journal citation and DOI.

Andersson et al. 2015). There has been an increasing number of dust polarization observations that reveal the POS magnetic field orientation in star-forming molecular clouds (Pattle & Fissel 2019; Hull & Zhang 2019). The Davis-Chandrasekhar-Fermi (DCF) method (Davis 1951; Chandrasekhar & Fermi 1953) and its modified forms have been the most widely used methods to indirectly derive the magnetic field strength with statistics of field orientations. The compilation of previous DCF estimations suggests that magnetically trans-to-supercritical and averagely trans-to-super-Alfvénic clumps/cores form in subcritical clouds (Liu et al. 2022a). However, the breakdown of the DCF assumptions, such as energy equipartition (Skalidis & Tassis 2021) or turbulence isotropy (Lazarian et al. 2022), in specific physical conditions (e.g., in non-self-gravitating media) might bring some uncertainties to the DCF estimations (see a review of the DCF method in Liu et al. 2022b). Thus, it is essential to study the magnetic field properties with other statistical methods as well.

Well-ordered magnetic field structures (e.g., hourglass or toroidal shapes) are seldom observed in star-forming regions (see a review of observed hourglass-shaped magnetic fields in Hull & Zhang 2019). Many star formation regions show complex magnetic field structures, which cause difficulties in interpreting the field topology. The development of statistical techniques has made it possible to infer the physical properties of star formation regions by comparing the magnetic field orientation with other orientations (e.g., the column density gradient/column density contour/intensity gradient, 13 the direction of local gravity, and the velocity gradient) that can be obtained through astronomical observations. For instance, the Histogram of Relative Orientation analysis (HRO; Soler et al. 2013) measures the statistical relation between magnetic fields and density structures, and it can be used to link the physical properties of observations and simulations. The observational HRO studies reveal that the magnetic field and column density contour change from a preferential parallel alignment to a perpendicular alignment with increasing column densities (e.g., Planck Collaboration et al. 2016), and they may transit back to a random alignment at higher column densities (e.g., Beuther et al. 2020; Kwon et al. 2022). The observational trends suggest that star formation is ongoing in trans-to-sub-Alfvénic clouds, and the magnetic field is likely affected by star formation activities in high-density regions. However, the exact reason for the different alignment at different column densities is still under debate (see a review of the HRO analysis in Liu et al. 2022b). On the other hand, the polarization-intensity gradient method (Koch-Tang-Ho or KTH method; Koch et al. 2012a) proposes to determine the local magnetic field strength as well as the local normalized mass-to-flux ratio (λ_{KTH}) under the assumption of ideal magnetohydrodynamics (MHD) by comparing the local orientations of magnetic fields, intensity gradients, and local gravity. Several observational KTH studies found that the magnetic field strength or λ_{KTH} estimated with the KTH method are not far from the DCF estimations (e.g., Stephens et al. 2013; Girart et al. 2013; Añez-López et al. 2020). A review of all the observational KTH studies can be found in Liu et al. (2022b). Moreover, the velocity gradients from molecular line observations are expected to be perpendicular to the local magnetic field orientation in the absence of gravity, due to the intrinsic property of MHD turbulence, where the correlation between the magnetic field and velocity gradient should be weaker for larger Alfvénic Mach numbers (Gonzalez-Casanova & Lazarian 2017; Lazarian & Yuen 2018). In high-density regions, the infalling gas due to strong self-gravity may drag the magnetic field lines and align magnetic fields with velocity gradients, where the alignment may be used to identify self-gravitating regions (Yuen & Lazarian 2017a, 2017b). A synergistic analysis with these techniques using relative orientations between different angles will be advantageous in revealing the physical conditions in star-forming molecular clouds.

The massive (> $10^5 M_{\odot}$) star-forming complex NGC 6334 at a distance of ~1.3 kpc (Wu et al. 2014; Chibueze et al. 2014) is one of the nearest massive star-forming regions from the Sun, and it has been extensively studied at various wavelengths (see a review by Persi & Tapia 2008). The predominant structure in the NGC 6334 complex is a 10 pc long filamentary cloud (hereafter the NGC 6334 cloud or NGC 6334 filament)

elongated along the direction of the galactic plane. The NGC 6334 filament harbors six massive star-forming molecular clumps (N6334I-V and N6334I(N)) that were identified with far-infrared/submm/mm observations (e.g., Cheung et al. 1978; McBreen et al. 1979; Gezari 1982). The high-luminosity (>10^4L_{\odot}), large gas reservoir, presence of H₂O, OH, and CH₃OH (class I and II) masers, and detections of compact and ultracompact H II regions, outflows, young stellar objects, and massive stars within or in the vicinity of these clumps suggest that these clumps are undergoing active intermediate- to highmass star formation (e.g., Rodriguez et al. 1982; Loughran et al. 1986; Munoz et al. 2007; Persi & Tapia 2008; Russeil et al. 2012; Willis et al. 2013; Andre et al. 2016).

The magnetic field structure of the NGC 6334 region at different scales has been previously studied with dust polarization observations (Zhang et al. 2014; Li et al. 2015; Juarez et al. 2017; Arzoumanian et al. 2021; Palau et al. 2021; Cortes et al. 2021). Specifically, the multi-scale magnetic field study by Li et al. (2015) revealed that the orientation of magnetic fields does not change much from cloud scales to clump and core scales in N6334I and I(N), where the areaaveraged magnetic field is perpendicular to the area-averaged elongation of density structures at each scale. This signifies a dynamically important role played by magnetic fields on guiding gravitational collapse, which leads to a self-similar fragmentation across various scales. Different trends have been found in some subregions (N6334IV and V) where the magnetic fields might be affected by stellar feedback or converging flows (Li et al. 2015; Juarez et al. 2017). In addition, Arzoumanian et al. (2021) found that the magnetic field changes from being perpendicular or randomly aligned with the outer part of the subfilaments to being parallel to the inner part of the subfilaments that merges into the main filament, which may indicate infalling gas flows from subfilaments to the main filament.

In this paper, we present high-resolution (~900 au) Atacama Large Millimeter/submillimeter Array (ALMA) 1.3mm dust polarization and molecular line observations toward clumps N6334I(N), I, IV, and V in NGC 6334 to study the physical properties within molecular dense cores. We also collect the historical dust polarization data and molecular line data at coarser resolutions for the study of the large-scale physical conditions at cloud and clump scales. In Section 2, we describe the observational data. In Section 3, we present maps of the density structure, magnetic field structure, and velocity structure. In Section 4, we study the relative orientations between magnetic fields, column density gradients, local gravity, and velocity gradients at different column densities, and we discuss their implication on the physical properties in NGC 6334. A summary of this paper is provided in Section 5. We only focus on the statistical properties of physical conditions at different scales in this paper, and we will present detailed analyses of ALMA observations toward individual clumps in future papers.

2. Observation

2.1. ALMA Dust Polarization and Molecular Line Observations

Four clumps (N6334I(N), I, IV, and V) in the massive cloud NGC 6334 were observed with ALMA on 2018 June 28 (in C43-1 configuration) and 2018 September 2 (in C43-4 configuration) under the project 2017.1.00793.S (PI: Qizhou

¹³ The column density gradient is perpendicular to the column density contour. The column density gradient is parallel to the intensity gradient if the physical parameters of gas and dust are constant or their variations are along the density gradient.

Table 1
Source Coordinates of ALMA Observations

Source	Field	$\alpha_{ m J2000}$	$\delta_{ m J2000}$
N6334I	NGC6334I	17 ^h 20 ^m 53 ^s 41	-35°46′57″ 8
N6334I(N)	NGC6334In.1	17 ^h 20 ^m 54 ^s 97	-35°45′05″ 6
	NGC6334In.2	17 ^h 20 ^m 54 ^s 53	-35°45′18″ 8
	NGC6334In.3	$17^{\text{h}}20^{\text{m}}56\stackrel{\text{s}}{.}00$	-35°45′27″ 5
N6334IV	NGC6334IV.1ª	17 ^h 20 ^m 19 ^s 72	-35°54′38″ 0
	NGC6334IV.2 ^a	$17^{h}20^{m}18\stackrel{s}{.}24$	-35°54′42″ 7
	NGC6334IV.3 ^a	17 ^h 20 ^m 18 ^s .19	-35°54′52″. 7
N6334V	NGC6334V	17 ^h 19 ^m 57 ^s 55	-35°57′50″ 8

Note.

Zhang). Tables 1 and 2 list the detailed information of the observations. The correlator was configured in the full polarization mode in ALMA band 6 with three spectral windows to cover the dust continuum at \sim 215.5219.5 GHz and \sim 232.5234.5 GHz, and four spectral windows to cover the 12 CO (2–1), OCS (19–18), 13 CS (5–4), and N_2D^+ (3–2) lines. The three spectral windows covering the dust continuum have a total bandwidth of 5.6 GHz (three basebands, with 1.875 GHz effective bandwidth each). The line spectral windows have a channel width of 122 kHz (0.16 km s $^{-1}$) over a bandwidth of 58.6 MHz (\sim 76 km s $^{-1}$).

The data were calibrated by the ALMA supporting staff with Common Astronomy Software Applications (CASA; McMullin et al. 2007). We performed two rounds of phase-only selfcalibration on the manually extracted line-free channels of the Stokes I data for the dust continuum using CASA. We imaged the molecular line cubes and Stokes I, Q, and U maps of dust continuum using the CASA task TCLEAN with a Briggs weighting parameter of robust =0.5. The maps for N6334I(N) and N6334IV were each constructed from three-pointing mosaics. The synthesized beam of the combined (C43-1 plus C43-4) images is $\sim 0.77 \times 0.75$ ($\sim 0.004-0.003$ pc or $\sim 900-700$ au at a distance of 1.3 kpc). The maximum recoverable scale 14 is $\sim 13''$ (\sim 0.08 pc at 1.3 kpc). Before primary beam correction, the 1σ root-mean-square (rms) noises were ~ 0.8 , 3.8, 0.6, and 0.8 mJy beam⁻¹ for the Stokes I dust continuum maps and ~ 0.08 , 0.09, 0.05, and 0.06 mJy beam⁻¹ for the Stokes Q or U dust continuum maps of N6334I(N), I, IV, and V, respectively. The debiased polarized intensity PI and its corresponding uncertainty σ_{PI} are calculated as $PI = \sqrt{Q^2 + U^2 - \sigma_{QU}^2}$ (Vaillancourt 2006) and $\sigma_{PI} \sim \sqrt{2} \, \sigma_{QU}$, where σ_{QU} is the 1σ rms noise on the background region $(Q \sim U \sim 0)$ of the Q or U maps. The polarization position angle θ_p is estimated with $\theta_p =$ 0.5 $\arctan(U/Q)$. The uncertainty on the polarization position angle (Naghizadeh-Khouei & Clarke 1993) is given by $\delta\theta = 0.5 \sqrt{\sigma_{OU}^2/(Q^2 + U^2)} \sim 20^{\circ}.26(\sigma_{PI}/PI) \sim 28^{\circ}.65(\sigma_{QU}/PI),$ where we assume σ_{OU} is not far from the observational error of Q and U (i.e., δQ and δU). The rms noises of the spectral line cubes (before primary beam correction) with a velocity channel width of 0.16 km s⁻¹ are \sim 3.8, 8.7, 3.0, and 5.2 mJy beam⁻¹ for N6334I(N), I, IV, and V, respectively. We also imaged

several CH₃OH lines in the low-resolution continuum spectral windows to derive the gas temperature with the rotation diagram analysis (see Appendix C). All the ALMA images shown in this paper are before primary beam correction. The continuum fluxes used for the column density estimation in Appendix C are after primary beam correction.

2.2. JCMT 850 µm Dust Polarization and ¹³CO (3-2) Data

We adopt the 850 μ m (\sim 353 GHz) I. O. and U images observed with SCUBA-2/POL-2 (Holland et al. 2013; Friberg et al. 2016) on the James Clerk Maxwell Telescope (JCMT) at a resolution of \sim 14" (\sim 0.09 pc) toward the whole NGC 6334 filamentary cloud. The JCMT data (program code: M17BL011) were previously published by Arzoumanian et al. (2021) as part of the JCMT large program B-field In STar-forming Region Observations (BISTRO: Ward-Thompson et al. 2017). For areas with signal-to-noise ratios (S/Ns) greater than 25 for the I map, the mean values for the observational error of *I*, *Q*, and *U* (i.e., δI , δQ , and δU) are ~ 1.6 , 1.13, and 1.6 mJy beam $^{-1}$, respectively (Arzoumanian et al. 2021). The debiased polarized intensity PI and its corresponding error 15 δPI are calculated as $PI = \sqrt{Q^2 + U^2 - 0.5(\delta Q^2 + \delta U^2)}$ and $\delta PI = (Q\delta Q + U\delta U)/\sqrt{Q^2 + U^2} \sim \sqrt{(Q^2\delta Q^2 + U^2\delta U^2)/(Q^2 + U^2)},$ respectively. The polarization position angle and its uncertainty $\delta\theta$ (Naghizadeh-Khouei & Clarke 1993) estimated with $\theta_p = 0.5 \arctan(U/Q)$ and $\sqrt{(Q^2\delta U^2 + U^2\delta Q^2)/(Q^2 + U^2)^2} \sim 28^{\circ}.65(\delta PI/PI),$ respectively, where we assume $\delta PI \sim \delta O \sim \delta U$.

Additionally, we include in our analysis the 13 CO (3–2) line cubes toward N6334I(N) and N6334I taken with the Heterodyne Array Receiver Program and Auto-Correlation Spectrometer and Imaging System (HARP and ACSIS; Buckle et al. 2009) from the JCMT data archive (program code: M11BN07). The spatial and spectral resolutions of the 13 CO (3–2) data are \sim 14" and 0.055 km s $^{-1}$, respectively. The map size is $2' \times 2'$ (\sim 0.76 pc \times 0.76 pc) for each field. The rms noises of N6334I (N) and N6334I are 0.90 and 0.45 K per channel, respectively, in corrected antenna temperature ($T_{\rm A}^*$). The pipeline-produced data cubes in the barycentric velocity frame are converted to the kinematic local standard of rest (LSRK) radio velocity frame with Starlink (Currie et al. 2014). Because the two clumps are larger than the beam, we estimate the antenna radiation temperature ($T_{\rm R}^*$) from $T_{\rm A}^*$ adopting a forward efficiency 16 of $\eta_{\rm fss} = 0.75$.

2.3. Planck 353 GHz Dust Polarization Data

Planck maps toward the NGC 6334 region and its surrounding area observed with the High Frequency Instrument (HFI; Lamarre et al. 2010) at 353 GHz are included in our analysis to study the global-scale density structure and magnetic fields. We adopt the 353 GHz Stokes Q and U maps of the thermal dust emission (version R3.00; Planck Collaboration et al. 2020) constructed with the Generalized Needlet Internal Linear Combination method (GNILC; Remazeilles et al. 2011) and the earlier released dust optical depth (τ_{353}) and temperature maps (version R1.02; Planck Collaboration et al. 2014). The Planck maps are at a

^a There is a typo in the ALMA data archive. Field NGC6334VI in the archive should be NGC6334IV.

¹⁴ https://almascience.eso.org/observing/observing-configuration-schedule/prior-cycle-observing-and-configuration-schedule

 $[\]overline{^{15}}$ It should be noted that the propagated observational error δPI for the JCMT and Planck polarization map is position-dependent and is a different type of uncertainty than the rms noise σ_{PI} for the ALMA polarization map. There is $\delta PI \sim \delta Q \sim \delta U$ but $\sigma_{PI} \sim \sqrt{2} \, \sigma_{QU} \sim \sqrt{2} \, \delta Q \sim \sqrt{2} \, \delta U$.

 $^{^{16}\} https://www.eaobservatory.org/jcmt/instrumentation/heterodyne/harp/$

Table 2
Parameters of ALMA Observations

Date	Configuration	$N_{ m ant}^{-{ m a}}$	Bandpass Calibrator	Gain Calibrator	Flux Calibrator	Polarization Calibrator
2018 Jun 28	C43-1	47	J1751+0939	J1851+0035	J1751+0939	J1924-2914
2018 Sep 2	C43-4	44	J1924-2914	J1733-3722	J1924-2914	J1924-2914

Note.

resolution of 5' (\sim 1.9 pc). Within our considered map area, the mean values for the uncertainties of Q and U (i.e., δQ and δU) are \sim 3 and 4 μK_{CMB} , respectively. The debiased polarized intensity PI and its corresponding uncertainty δPI are calculated as $PI = \sqrt{Q^2 + U^2 - 0.5(\delta Q^2 + \delta U^2)}$ and $\delta PI \sim \sqrt{(Q^2 \delta Q^2 + U^2 \delta U^2)/(Q^2 + U^2)}$, respectively. The adopted Planck Q and U maps downloaded from the Planck Legacy Archive $\frac{1}{2}$ are in galactic coordinates. We estimate the polarization position angle in equatorial coordinates with $\theta_p = 0.5 \arctan(U/Q) - \Delta \theta_p^{g-e}$, where

$$\Delta\theta_{\rm p}^{\rm g-e} = \arctan\left(\frac{\cos(l-32\degree 9)}{\cos b \cot 62\degree 9 - \sin b \sin(l-32\degree 9)}\right) (1)$$

is the angle between the galactic and equatorial reference directions (Corradi et al. 1998). For NGC 6334 at $l=351^{\circ}.33$ and $b=0^{\circ}.68$, we adopt $\Delta\theta_{\rm p}^{\rm g-e}\approx55^{\circ}.22$. Similarly to the JCMT data, the uncertainty on the Planck polarization position angle is given by $\delta\theta\sim28^{\circ}.65(\delta PI/PI)$.

2.4. NANTEN2 ¹²CO (1–0) Data

We also include in our analysis the ^{12}CO (1–0) data from Fukui et al. (2018) to study the global-scale velocity fields. The data were obtained with NANTEN2, which is a 4 m millimeter/submillimeter radio telescope in Chile. The spatial and spectral resolutions of the ^{12}CO (1–0) cubes are $\sim 3'$ (~ 1.1 pc) and 0.16 km s $^{-1}$, respectively. The typical rms noise level is ~ 1.2 K per channel. In this study, the NANTEN2 ^{12}CO (1-0) data are convolved to a beam size of 5' to match the Planck resolution.

3. Results

3.1. Dust Continuum and Magnetic Fields

In this subsection, we briefly overview the multi-scale magnetic field structures in the NGC 6334 region traced by Planck, JCMT, and ALMA dust polarization observations. Assuming that the observed linear dust polarization is due to dust grain alignment, the dust polarization position angle is rotated by 90° to reveal the magnetic field orientation. It is possible that the observed polarization of the ALMA dust emission peaks is affected by other possible dust polarization mechanisms (e.g., disk self-scattering or dichroic extinction; see Girart et al. 2018; Liu 2021). But these mechanisms that are predominant at scales smaller than 100–200 au should not be significant for our ALMA observations with a resolution of ~900 au.

Figure 1(a) shows the magnetic field orientation of the NGC 6334 complex traced by Planck dust polarization observations, which has been briefly reported by Arzoumanian et al. (2021).

The well-ordered magnetic fields in the diffuse region surrounding NGC 6334 mostly show a northeast–southwest orientation, which tends to be parallel to the galactic plane and the NGC 6334 filament. Toward the 10 pc long predominant NGC 6334 filament, the magnetic field in the northern part (containing N6334I(N) and N6634I) of the filament changes to be mostly perpendicular to the main filament and is pinched toward the northern end. The magnetic field in the southern part (containing N6334IV and N6634V) of the filament also deviates from the global-scale magnetic field and changes to a north–south orientation.

Figure 1(b) shows the JCMT BISTRO observations of the magnetic field orientation in the NGC 6334 filament (Arzoumanian et al. 2021). The magnetic field near N6334I and N6334I(N) is mostly perpendicular to the filament and shows dragged-in structures toward the north of N6334I(N) and the south of N6334I, which agrees with the large-scale magnetic field revealed by Planck. The magnetic field in N6334IV and N6334V shows complex structures without a prevailing orientation.

Our ALMA polarization observations have revealed the continuum emission structures and magnetic field structures in the four massive clumps (N6334I(N), I, IV, and V) down to a resolution of <1000 au. Figure 2 shows the ALMA observational results of the magnetic field orientation in the four clumps. Clump N6334I(N) is resolved into three parallel 0.1–0.2 pc long elongated filamentary structures (hereafter I(N)-f1, f2, and f3, from north to south) that follow the direction of the N6334 main filament and are perpendicular to the clump-scale magnetic field revealed by JCMT. Each 0.1 pc scale filament fragments into a group of compact sources. The magnetic field in the predominant I(N)-f1 is overall perpendicular to the direction of the elongation and shows pinched (or hourglass) field morphology, which agrees with the previous ALMA polarization observations with poorer sensitivity (Cortes et al. 2021). The magnetic fields in I(N)-f2 and I(N)f3 are more complex, which might be due to them being affected by turbulence or (proto-)stellar feedback. In N6334I, the dominant 0.1 pc core (I-c1) fragments into a cluster of compact sources. The magnetic field in the core shows radial patterns in the outer region, pinched structures near fainter emission peaks, and spiral-like structures near the brightest emission peak, which deviates from the coherent and approximately straight field at cloud and clump scales (Zhang et al. 2014; Li et al. 2015; Arzoumanian et al. 2021). The magnetic field pattern in core I-c1 seems to indicate that the field is dragged by gravity and influenced by core/disk rotation (e.g., Sanhueza et al. 2021). The radial field patterns in the outer region may be related to accretion streamers that are connected to the central core. Clump N6334IV is resolved into an elongated filamentary structure (IV-f1) containing several compact sources in the north and a core (IV-c1) in the south. In

a Number of antennas

¹⁷ http://pla.esac.esa.int/

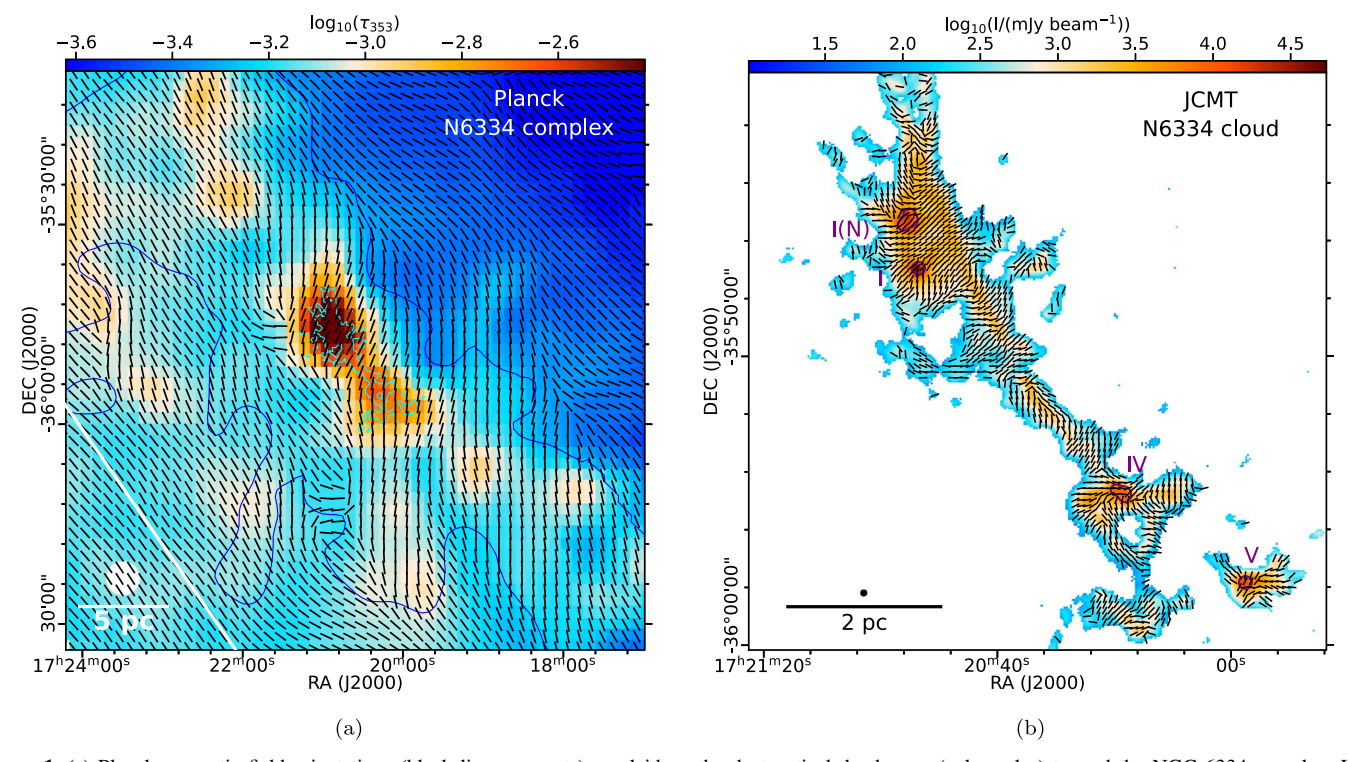


Figure 1. (a) Planck magnetic field orientations (black line segments) overlaid on the dust optical depth map (colorscales) toward the NGC 6334 complex. Line segments are of arbitrary length. All Planck polarization detections have signal-to-noise ratios (S/Ns) greater than 3. The 5' (\sim 1.9 pc) beam (white circle), a scale bar of 5 pc, and the galactic plane (white line) are indicated in the lower left corner. The 10 pc long NGC 6334 filament is elongated along the direction of the galactic plane. The cyan contour indicates the region with S/N(I) = 25 for the JCMT observation. The blue contour indicates the region with NANTEN2 integrated 12 CO (1–0) intensity greater than 25 K km s $^{-1}$ within which we perform the relative orientation analysis. (b) JCMT magnetic field orientations (black line segments) overlaid on the total intensity map of the dust emission (colorscales) toward the NGC 6334 filament from BISTRO observations (Arzoumanian et al. 2021). Line segments are of arbitrary length. Only line segments with S/N(I)>25 and S/N(I)>3 are shown. The 14'' (\sim 0.09 pc) beam (black circle) and a scale bar of 2 pc are indicated in the lower left corner. Purple contours indicate the Full Width at Half Maximum (FWHM) field of view of our ALMA observations.

the central part of IV-f1, the magnetic field is mostly along the elongation of IV-f1, which agrees with previous SMA polarization observations (Zhang et al. 2014). Around the two compact sources in the east and west ends of IV-f1, the magnetic field orientation shows bimodal distributions, which may suggest a magnetized collapse (Maury et al. 2018). The northern part of core IV-c1 shows a prevailing east-west magnetic field orientation, while the southern part shows a prevailing north-south orientation. Clump N6334V is resolved into two nearly parallel elongated structures (V-f1 and V-f2 from north to south) connected with each other in the western part. The magnetic field in V-f2 shows a dominant east—west orientation, which follows the elongation of V-f2 and agrees with previous SMA observations (Juarez et al. 2017). The magnetic field also shows a radial pattern in the eastern end of V-f2 and signs of pinched structure in the western end. The magnetic field in V-f1 is overall complex but shows wellordered and consistent field in some subregions.

3.2. Molecular Lines and Velocity Fields

We use NANTEN2 12 CO (1–0), JCMT 13 CO (3–2), and ALMA OCS and 13 CS data to study the kinematics at different scales. In this subsection, we briefly overview the multi-scale intensity-weighted velocity (moment 1 or velocity centroid V_c) structures (Figures 3 and 4) in the NGC 6334 region. The integrated intensity (moment 0) maps of these lines are shown in Appendix A. The velocity centroid $V_c(x)$ at position x is

calculated with

$$V_c(\mathbf{x}) = \frac{\sum_{i}^{N_{\text{ch}}} I_i(\mathbf{x}) \nu_i \Delta \nu_{\text{ch}}}{\sum_{i}^{N_{\text{ch}}} I_i(\mathbf{x}) \Delta \nu_{\text{ch}}},$$
(2)

where $I_i(x)$, v_i , $\Delta v_{\rm ch}$, and $N_{\rm ch}$ are the line intensity, line-of-sight velocity, channel width, and number of integrated channels, respectively. The propagated uncertainty of the calculated velocity centroid is given by (Dickman & Kleiner 1985; Teague 2019)

$$\delta V_c(\mathbf{x}) = \frac{\sigma_{\rm ch} \Delta v_{\rm ch} \sqrt{\sum_i^{N_{\rm ch}} (v_i - V_c(\mathbf{x}))^2}}{\sum_i^{N_{\rm ch}} I_i(\mathbf{x}) \Delta v_{\rm ch}},$$
(3)

where $\sigma_{\rm ch}$ is the noise of one spectral channel (reported in Section 2). For the NANTEN2 ¹²CO (1–0) and JCMT ¹³CO (3–2) observations, we only consider the line emission from – 12 to 4 km s⁻¹, because most of the large-scale line emission in the NGC 6334 region is within this velocity range (Arzoumanian et al. 2022). A second and fainter velocity component in the NGC 6334 region from –20 to –12 km s⁻¹ has been previously reported (Fukui et al. 2018) but is not considered in this work. At small scales and near young stellar objects, the outflow usually dominates at \gtrsim 5 km s⁻¹ (e.g., Qiu et al. 2009; Liu et al. 2018) with respect to the local standard of rest (LSR) velocity ($V_{\rm lsr}$) of the central source within massive star formation regions. The low-velocity (<5 km s⁻¹) outflowing gas is usually indistinguishable from the clump bulk gas. Thus,

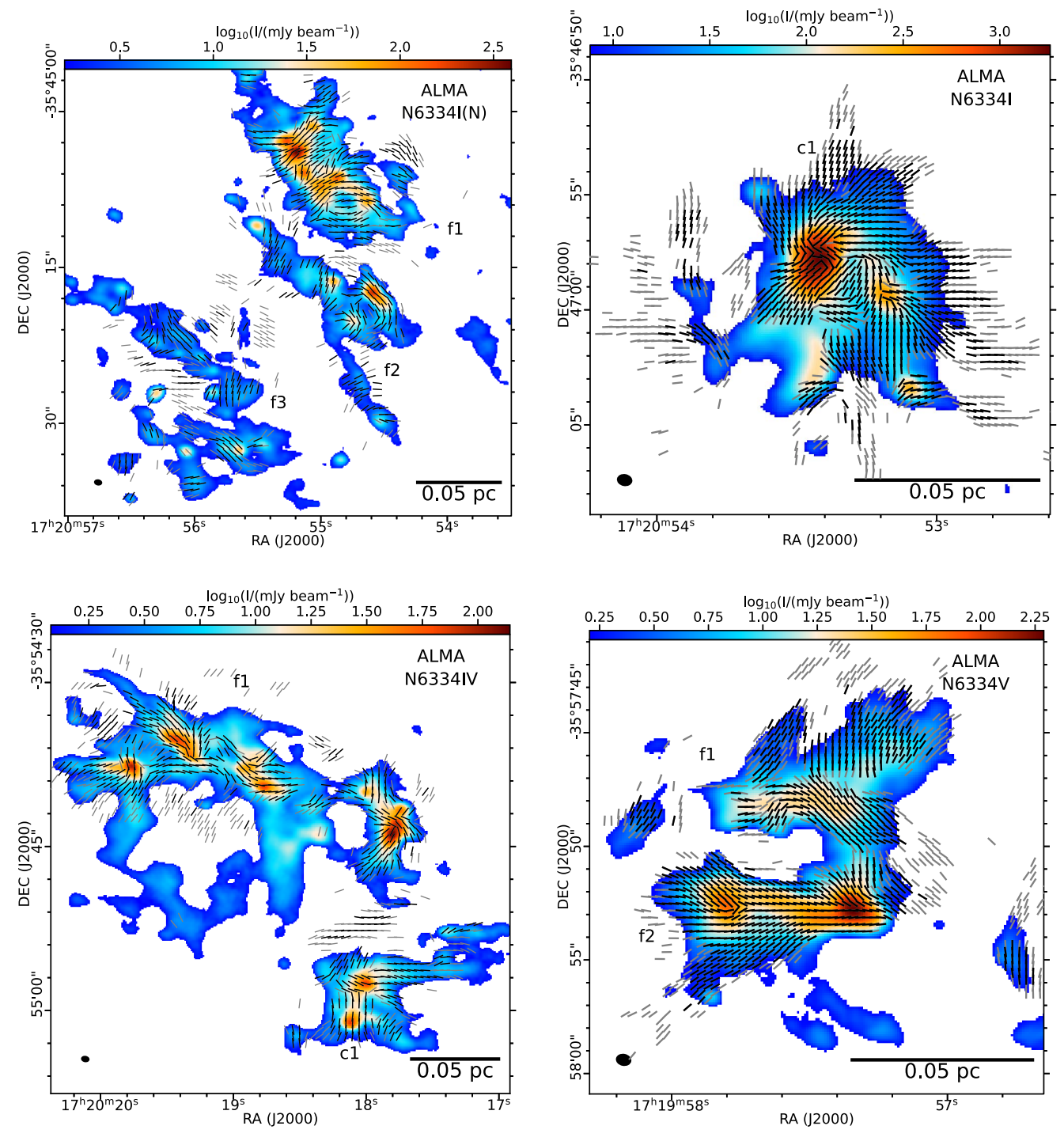


Figure 2. ALMA observations (C43-1 and C43-4 combined) toward the massive clumps N6334I(N), I, IV, and V. Magnetic field orientations (black and gray line segments indicate S/N(PI) > 3 and 2 < S/N(PI) < 3, respectively) are overlaid on the total intensity map (S/N(I) > 2) of the dust emission (colorscales). Line segments are of arbitrary length. The $\sim 0.77 \times 0.75$ ($\sim 0.004-0.003$ pc or $\sim 900-700$ au) synthesized beam (black ellipse) and a scale bar of 0.05 pc are indicated in the lower left and right corner of each panel, respectively.

we only consider velocities within \sim 5 km s⁻¹ with respect to the $V_{\rm lsr}$ of each clump for the ALMA OCS and 13 CS lines. The LSR velocities are \sim -3.5, -7.5, -3.5, and -6 km s⁻¹ for N6334I(N), I, IV, and V, respectively. In Figure 5, we indicate the considered velocity ranges for each clump on the averaged ALMA OCS and 13 CS spectra.

Figure 3(a) shows the velocity centroid map of the NGC 6334 complex traced by NANTEN2 ¹²CO (1–0) observations

(Fukui et al. 2018). The velocity structures of NGC 6334 and its surrounding material are coherent and there is a global velocity gradient of $0.1 \text{ km s}^{-1} \text{ pc}^{-1}$ from northeast to southwest along the direction of the galactic plane, but the origin of this global velocity gradient is still unclear (Arzoumanian et al. 2022).

Figures 3(b) and (c) show the velocity centroid map of N6334I(N) and I traced by JCMT ¹³CO (3–2) observations.

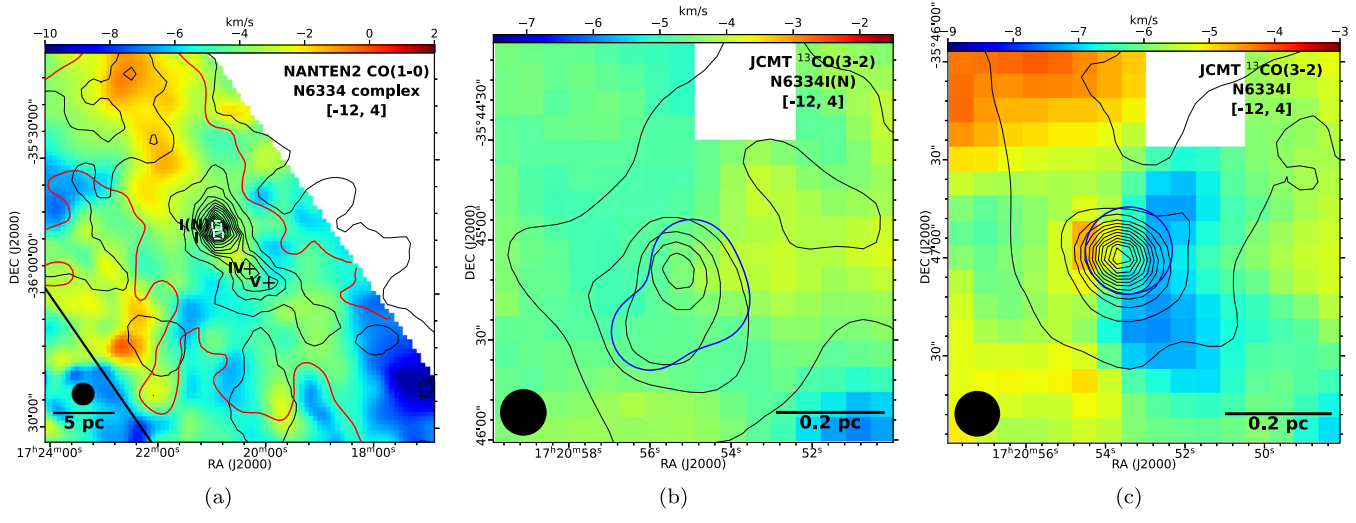


Figure 3. Panel (a) shows the velocity centroid map of NANTEN2 12 CO (1–0) line emission toward NGC 6334 complex (Fukui et al. 2018). The line data are convolved to a beam size of 5'. The black contour levels correspond to the Planck 353 GHz optical depth (τ_{353}) map. The contour starts at 0.0004 and continues with an interval of 0.0004. The white rectangles indicate the map area of the JCMT fields toward N6334I(N) and I in (b) and (c). Black crosses indicate the positions of N6334IV and V. The red contour indicates the region with NANTEN2 integrated 12 CO (1–0) intensity greater than 25 K km s $^{-1}$ within which we perform the relative orientation analysis. Panels (b) and (c) show velocity centroid maps of JCMT 13 CO (3–2) line emission toward N6334I(N) and N6334I. The black contour levels correspond to the JCMT 850 μm dust continuum map. Contour starts at 2 Jy beam $^{-1}$ and continues with an interval of 4 Jy beam $^{-1}$. Blue contours show the FWHM field of view of our ALMA observations.

The velocity centroid variation is small in N6334I(N), which might be because this clump is at an early star formation stage (Persi & Tapia 2008). There is a large-scale velocity gradient from northeast to southwest in N6334I, which agrees with the global velocity gradient seen in Figure 3(a).

Figure 4 shows the velocity centroid map of N6334I(N), I, IV, and V traced by ALMA OCS and ¹³CS observations. The velocity centroid maps of the two lines are very similar. In N6334I(N)-f1, there is a clear gradient from northeast to southwest, which should have a local origin at core scales, given that this gradient is not seen in JCMT observations at clump scales (Figures 3(b)). The gradient is reversed near the southwest edge of N6334I(N)-f1, which may indicate local converging flows. In N6334I, the dominating northeast-southwest velocity gradient agrees with the large-scale and globalscale velocity gradients seen by JCMT and NANTEN2 (Figure 3). In N6334IV, the velocity centroid variation is relatively small compared to the other three clumps, and there are no clear signs of ordered velocity gradients. In N6334V-f2, there is a clear east-west gradient, and the gradient is reversed in the west edge, which agrees with previous SMA H¹³CO⁺ and CH₃OH observations at a resolution of 2" (Juarez et al. 2017). Juarez et al. (2017) interpreted this velocity structure as converging flows. In N6334V-f1, we do not find the east-west gradient previously reported by Juarez et al. (2017), which may be due to differences in the beam resolution, filtering scale, or line excitation condition between their observations and ours.

4. Relative Orientation Analysis and Discussion

The relative orientation between magnetic field (θ_B), gas column density gradient (θ_{NG}), local gravity (θ_{LG}), and velocity centroid gradient (θ_{VG}) and their varying trend with column density are informative of the physical conditions of star-forming regions (Koch et al. 2012a; Soler et al. 2013; Gonzalez-Casanova & Lazarian 2017). In NGC 6334, the information on the magnetic field orientation and its uncertainty is available from the dust polarization observation. We

implement a 3×3 Sobel kernel (e.g., Soler et al. 2013) on the column density maps (see Appendix C) and line moment 1 maps (see Section 3.2) to derive the column density gradient (θ_{NG}) and velocity centroid gradient $^{18}(\theta_{VG})$ at different positions. The uncertainties of the column density and velocity centroid gradients are calculated following Planck Collaboration et al. (2016). The calculation of the gradients and their uncertainties is described in detail in Appendix B. Considering the significant S/N and the rather uniformly distributed observational error for the dust continuum emission observations, the uncertainty on the orientation of the column density gradient should be negligible (e.g., Planck Collaboration et al. 2016). Taking into account the gas mass of pixels with S/N(I)>3 (see Appendix C), we calculate the map-wise 2D direction of local gravitational force (θ_{LG}) with the standard formula of gravitation (e.g., Koch et al. 2012a; Liu et al. 2020). Calculating the uncertainty on the local gravity direction is time-consuming and we are unable to do so due to our limited computer resources.

Combining the approaches of the KTH method (Koch et al. 2012a) and the HRO analysis (Soler et al. 2013), we calculate and study the angular difference among these orientations. We use the alignment measure (AM) parameter introduced by the Velocity Gradient Technique (VGT, Gonzalez-Casanova & Lazarian 2017; Lazarian & Yuen 2018) to characterize the alignment between different orientations. The AM is given by

$$AM = \langle \cos(2\phi_{ol}^{o2}) \rangle, \tag{4}$$

where $\phi_{01}^{o2} = |\theta_{o1} - \theta_{o2}|$ is the angle between orientation 1 (θ_{o1}) and orientation 2 (θ_{o2}) and is in the range of 0°–90°. In the calculation of AM within each column density bin, different pixels are weighted equally. The AM is in the range of -1 (perpendicular) to 1 (parallel). AM > 0 (i.e., approximately

¹⁸ It should be noted that the term "velocity gradient" in our analysis refers to the local velocity gradient and is different from the subblock-averaged velocity gradient in the VGT.

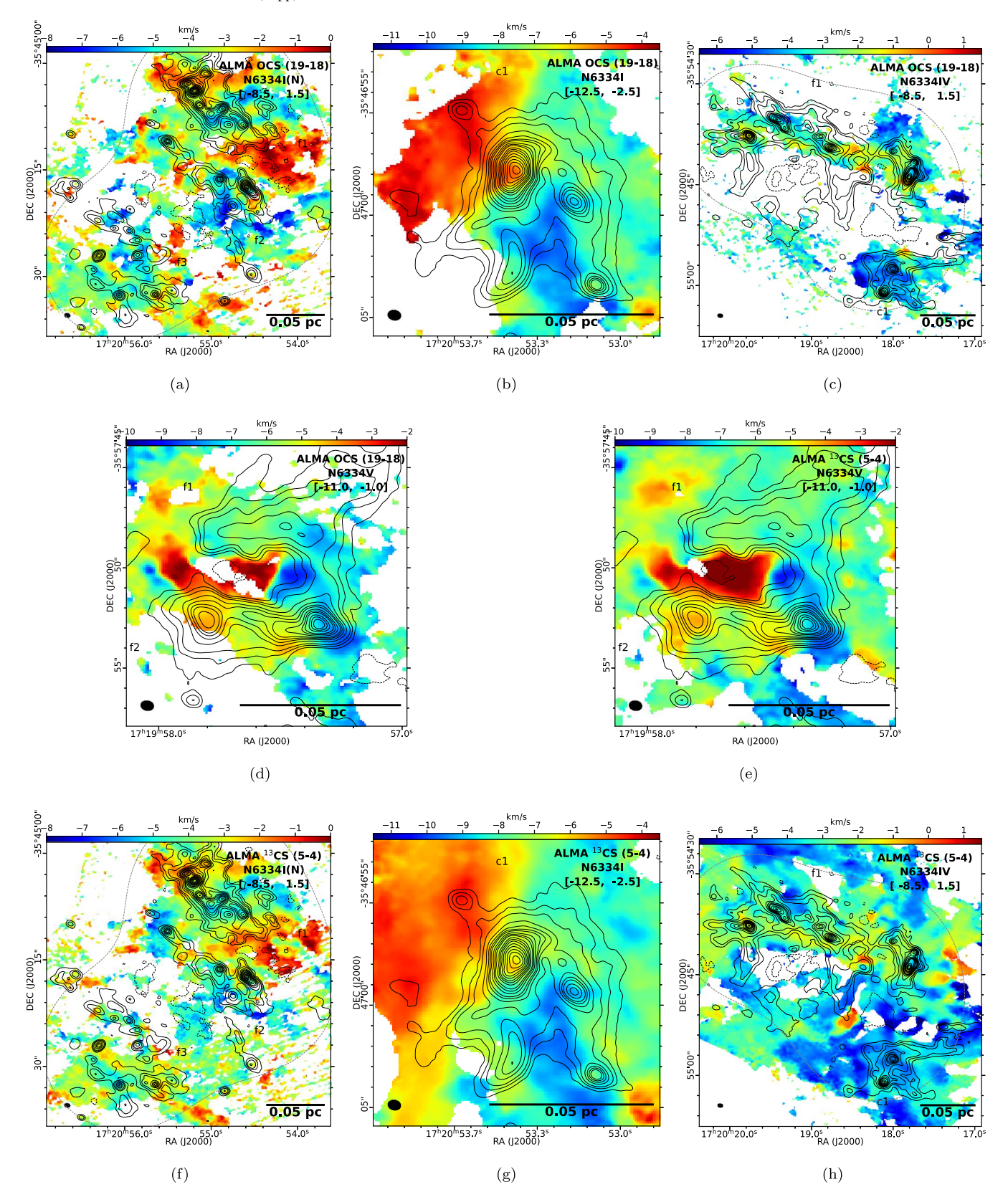


Figure 4. Velocity centroid maps of ALMA OCS ((a)–(d)) and 13 CS ((e)–(h)) observations. The black contour levels correspond to the ALMA dust continuum map. Contour levels are (± 3 , 6, 10, 20, 30, 40, 50, 70, 90, 110, 150, 180, 210, 250, 290, 340, 390, 450) $\times \sigma_I$, where σ_I is the rms noise of the Stokes I maps (see Section 2.1). Gray dashed contours correspond to the FWHM field of view of the ALMA observations.

 $\overline{\phi_{o1}^{o2}} < 45^{\circ}$) indicates two orientations are statistically more parallel than perpendicular in the considered region and vice versa. The uncertainty of ϕ_{o1}^{o2} is given by

 $\delta\phi_{\rm o1}^{\rm o2}=\sqrt{\delta\theta_{\rm o1}^2+\delta\theta_{\rm o2}^2}$. As discussed above, we adopt $\delta\theta=0$ for the column density gradient and gravity direction. We exclude data points with $\delta\phi>10^\circ$ in our analysis. The

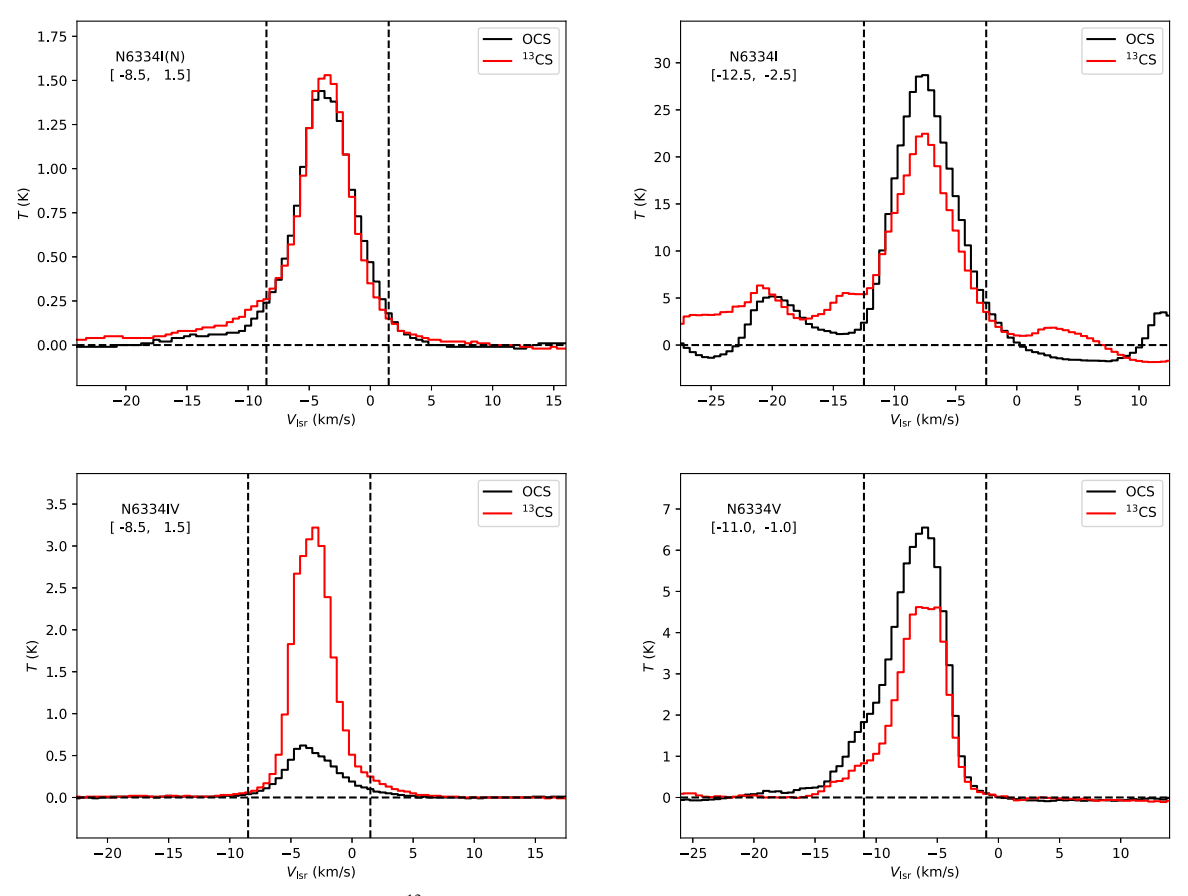


Figure 5. The averaged ALMA OCS (black histogram) and ¹³CS (red histogram) spectra of the considered area for each clump within which we perform the relative orientation analysis. The vertical dashed lines indicate the velocity range within which we calculate the integrated intensity and velocity centroid.

uncertainty of AM is given by (see Appendix B)

$$\delta AM = \sqrt{\left(\left\langle (\cos(2\phi_{o1}^{o2}))^2 \right\rangle - AM^2 + \sum_{i}^{n'} (2\sin(2\phi_i)\delta\phi_i)^2\right)/n'}, \tag{5}$$

where n' is the number of data points considered.

We calculate the AM for different relative orientations at different column densities. A NANTEN2 integrated ¹²CO (1–0) intensity of 25 K km s⁻¹ approximately separates the emission from the NGC 6334 complex and the background galactic plane emission (Fukui et al. 2018), and thus we exclude positions with NANTEN2 integrated ¹²CO (1-0) intensity smaller than 25 K km s⁻¹ for the Planck and NANTEN2 maps in our analysis. We consider every pixel with S/N > 3 detection in the JCMT and ALMA maps. Similarly to Planck Collaboration et al. (2016), we calculate AM in different $N_{\rm H_2}$ bins containing approximately equal number of pixels for each instrument (10, 15, and 15 $N_{\rm H_2}$ bins for Planck/ NANTEN2, JCMT, and ALMA, respectively). The typical numbers of pixels per bin¹⁹ are \sim 120–170, \sim 200–900, and ~200-1000 for Planck/NANTEN2, JCMT, and ALMA, respectively. We test and find that varying the number of $N_{\rm H_2}$ bins by a factor of 2 does not significantly affect the general trend on the relative orientation-column density (RO-N) relations. For the JCMT observation, we only derive the RO-

N relation for ϕ_{VG}^{B} , ϕ_{VG}^{NG} , and ϕ_{VG}^{LG} in N6334I(N) and N6334I in five N_{H_2} bins with \sim 20–50 pixels per bin. Figures 6, 7, 8, 9, 10, and 11 show the relative orientation between θ_B , θ_{NG} , θ_{LG} , and θ_{VG} characterized by AM as functions of column density. Because the atmospheric emission as well as the extended emission outside of the S/N-based masks (ASTMASK and PCAMASK) in the data reduction process are filtered out for POL-2 observations and the ALMA observation filters the extended spatial emission limited by the minimal separation of antenna pairs, the JCMT and ALMA observations can underestimate the actual column density. For NGC 6334, the JCMT observation filters out the large-scale emission corresponding to $N_{\rm H_2} \sim 3 \times 10^{22}~\rm cm^{-2}$ (Arzoumanian et al. 2021). Our ALMA observation filters out large-scale emissions at scales of >0.08 pc, but the filtered column density at this scale is unclear. Thus, the AM at the similar $N_{\rm H_2}$ but from different instruments are not comparable. On the other hand, the highest $N_{\rm H_2}$ bin of Planck/NANTEN2 observations contains the area of the NGC 6334 filament covered by the JCMT observation, and the highest $N_{\rm H_2}$ bin of JCMT observations contains the area of N6334I(N), I, IV, and V covered by the ALMA observation. Thus, we should regard the Planck/NANTEN2, JCMT, and ALMA observations as tracing low, intermediate, and high column densities, respectively.

4.1. Column Density Gradient versus Local Gravity

The relative orientation between column density gradient and local gravity (ϕ_{LG}^{NG}) may indicate how effectively gravity can shape the density structure.

¹⁹ The number of pixels per bin varies for different relative orientations, due to the different detection area for the total dust emission, polarized dust emission, and molecular line emission.

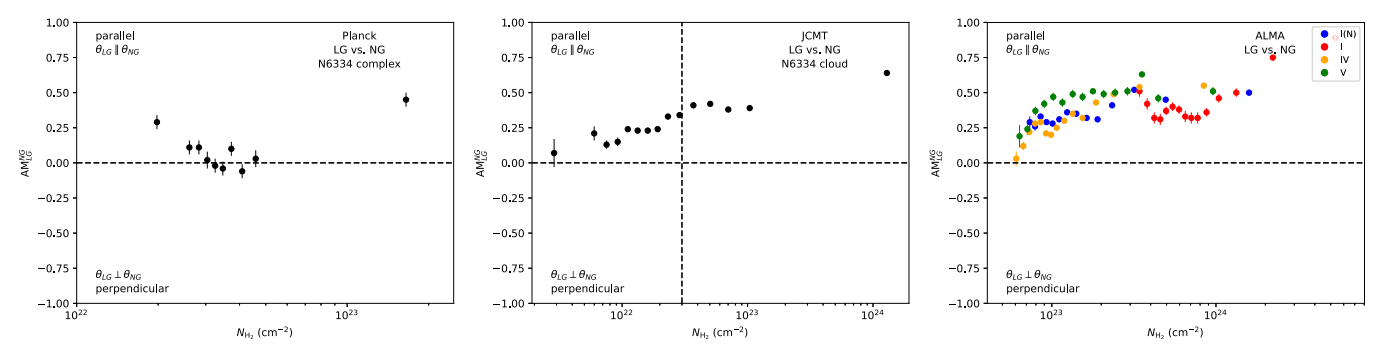


Figure 6. Relative orientations (characterized by AM; see Equation (4)) between column density gradient (θ_{NG}) and local gravity (θ_{LG}) as a function of column density for Planck (left), JCMT (middle), and ALMA (right) observations. Different colors indicate different clumps. The JCMT observation filters out the large-scale emission corresponding to $N_{H_2} \sim 3 \times 10^{22}$ cm⁻² (Arzoumanian et al. 2021), which is indicated by the vertical dashed line. The ALMA observation filters out the large-scale emission at scales >0.08 pc. The highest N_{H_2} bin of Planck observations contains the area of the NGC 6334 filament covered by the JCMT observation. The highest N_{H_2} bin of JCMT observations contains the area of the N6334I(N), I, IV, and V covered by the ALMA observation. The absolute column densities from different instruments are not comparable. Planck, JCMT, and ALMA observations trace low, intermediate, and high column densities, respectively. AM > 0 and AM < 0 indicate statistically more parallel and perpendicular alignments, respectively.

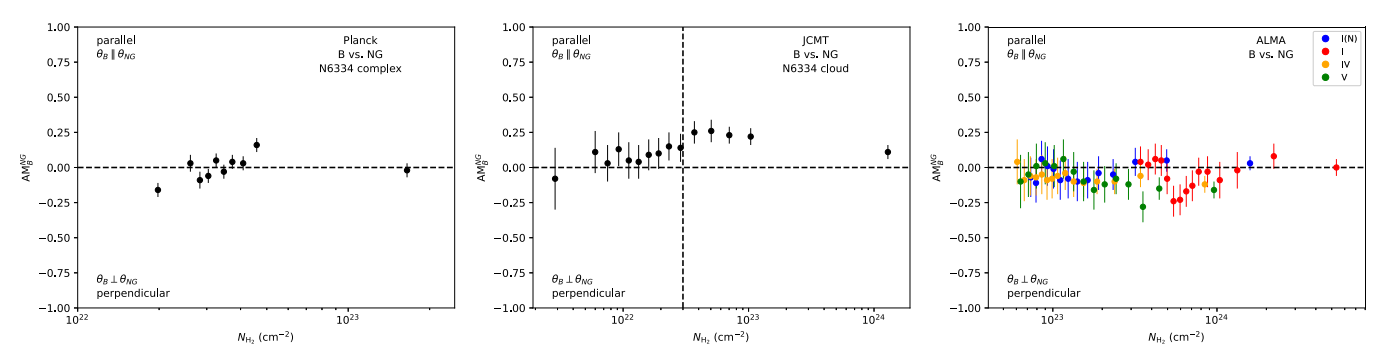


Figure 7. Same as Figure 6, but for the relative orientation between magnetic field (θ_B) and column density gradient (θ_{NG}).

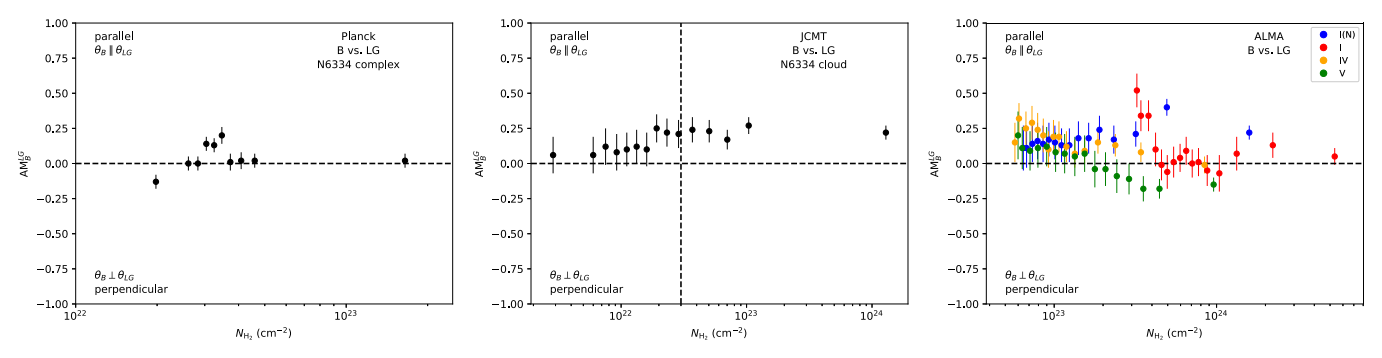


Figure 8. Same as Figure 6, but for the relative orientation between magnetic field (θ_B) and local gravity (θ_{LG}) .

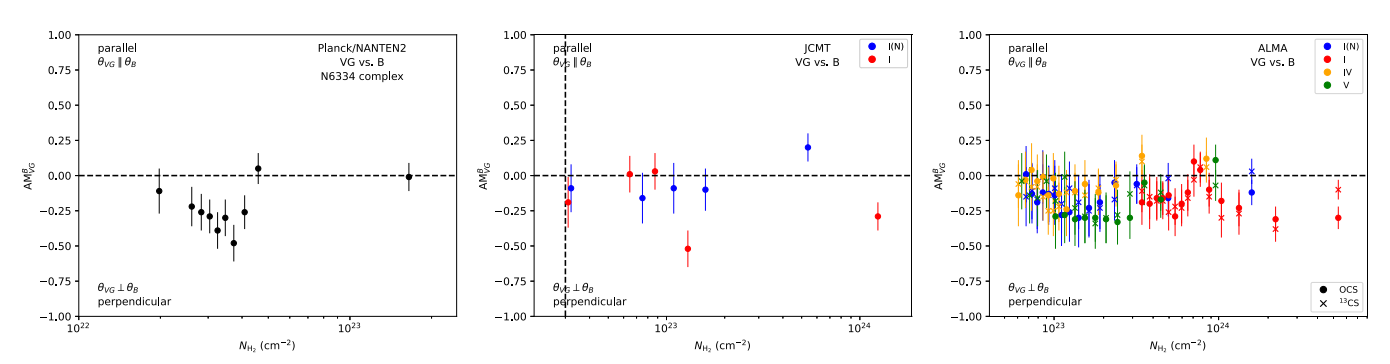


Figure 9. Same as Figure 6, but for the relative orientation between velocity gradient (θ_{VG}) and magnetic field (θ_B).

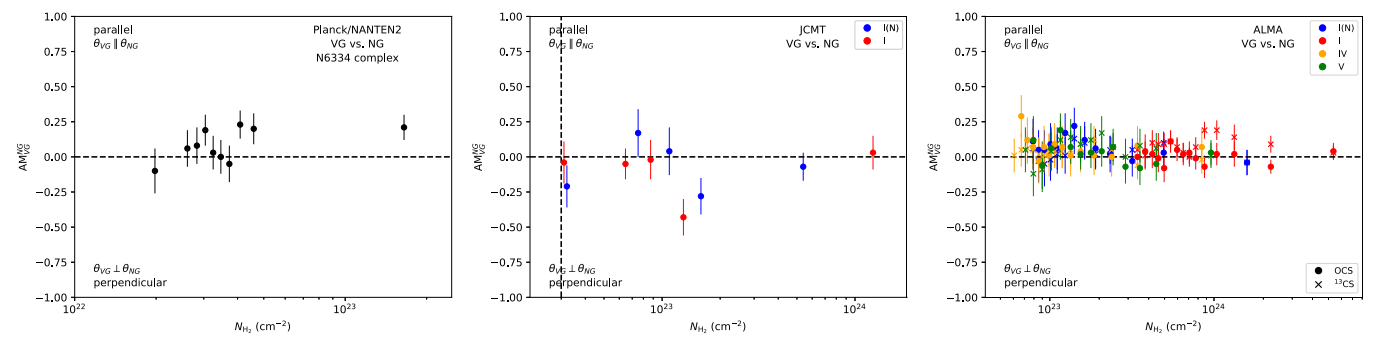


Figure 10. Same as Figure 6, but for the relative orientation between velocity gradient (θ_{VG}) and column density gradient (θ_{NG}).

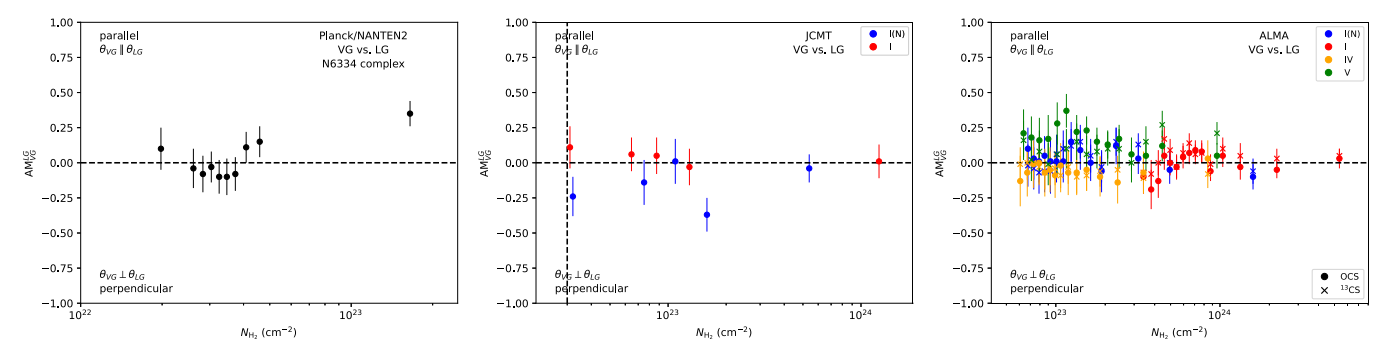


Figure 11. Same as Figure 6, but for the relative orientation between velocity gradient (θ_{VG}) and local gravity (θ_{LG}).

Figure 6 shows the RO–N relation for ϕ_{LG}^{NG} . For the Planck observation, there is AM \sim 0 in most N_{H_2} bins, but the value of AM is clearly positive in the lowest and highest N_{H_2} bins. While the highest N_{H_2} bin corresponds to the NGC 6334 main filament, the AM > 0 at the lowest N_{H_2} bin may just be a coincidence of specific geometry, because the gravity is not expected to be significant in diffuse regions. At the higher densities revealed by JCMT and ALMA, the two angles are always statistically more parallel than perpendicular (AM > 0). For the JCMT observation toward the whole filament, we see that AM increases with N_{H_2} . For ALMA observations toward individual clumps, the trend of increasing AM with N_{H_2} persists. Thus, we suggest that gravity plays an increasingly important role in shaping the density structure at higher densities.

4.2. Magnetic Field versus Column Density Gradient

The angle between the magnetic field and column density gradient $(\phi_B^{\rm NG})$ is complementary to the angle between the magnetic field and column density contour $(\phi_B^{\rm N})$ that has been extensively studied by the HRO analysis²⁰ both observationally (e.g., Planck Collaboration et al. 2016; Beuther et al. 2020; Kwon et al. 2022) and numerically (e.g., Soler et al. 2013, 2017; Seifried et al. 2020; Girichidis 2021). A detailed review of the observational and numerical HRO studies can be found in Liu et al. (2022b).

Figure 7 shows the RO–N relation for ϕ_B^{NG} from the Planck, JCMT, and ALMA observations. For the Planck observation, the overall statistical trend is that the magnetic field and column

density gradient change from a statistically slightly more perpendicular alignment (AM_B^{NG} $\lesssim 0$) at lower column densities to a slightly more parallel alignment (AM_B^{NG} $\gtrsim 0$) at higher column densities. At the highest $N_{\rm H_2}$ bin, the alignment measure of two angles transits back to $AM_B^{NG} \sim 0$ (i.e., no preferred orientation), which might be due to insufficient resolution. The transition from $AM_B^{NG} < 0$ to $AM_B^{NG} > 0$ is in agreement with trans-to-sub-Alfvénic simulations in numerical HRO studies (see a review in Liu et al. 2022b), which suggests the NGC 6334 is trans-to-sub-Alfvénic at complex/cloud scale. Similar trans-to-sub-Alfvénic states have been reported in the Gould Belt clouds from previous observational HRO and VGT studies (Planck Collaboration et al. 2016; Hu et al. 2019). The statistically more perpendicular alignment between the magnetic field and column density gradient (i.e., more parallel alignment between the magnetic field and column density contour) at low column densities may be due to the stretch of an initially super-Alfvénic turbulence or due to the intrinsic property of a large-scale sub-Alfvénic turbulence (see Liu et al. 2022b, and references therein). The direct reason for the transition from $AM_B^{NG} < 0$ to $AM_B^{NG} > 0$ is still under debate (Liu et al. 2022b). We refrain from deriving the transition column density for $AM_B^{NG} \sim 0$, due to the uncertainty of our estimated column densities (see Appendix C) and the inconsistency of absolute column densities between different instruments. At intermediate column densities revealed by JCMT, the two angles are mostly statistically more parallel (AM > 0). The value of AM_B^{NG} increases with $N_{\rm H_2}$ and then decreases with $N_{\rm H_2}$. Because the NGC 6334 region also tends to be trans-to-sub-Alfvénic at intermediate and high column densities (see discussions in Section 4.4 below), the more parallel alignment at this $N_{\rm H_2}$ range cannot be due to a local super-Alfvénic turbulence as proposed by some numerical studies (e.g., Chen et al. 2016); it is more likely due to the interaction between the magnetic field and local gravity (see

 $[\]overline{^{20}}$ The alignment measure parameter (AM $_B^{NG}$) for the magnetic field and column density gradient adopted by this work should not be confused with the HRO shape parameter (ξ ; Planck Collaboration et al. 2016) for the magnetic field and column density contour adopted by the HRO analysis. AM $_B^{NG} < 0$ approximately corresponds to $\xi > 0$, and vice versa.

discussions in Section 4.3 and Girichidis 2021). At even higher $N_{\rm H_2}$ bins revealed by ALMA, the alignment measure of two angles transits back to ${\rm AM_B^{NG}}\lesssim 0$ (i.e., no preferred orientation or slightly more perpendicular). The reason for the reverse transition is also unclear, but it may be related to the impact of converging gas flows, outflows, disk rotation, and/or the projection effect (Liu et al. 2022b). It should be noted that our results do not conflict with those of Li et al. (2015), who have found that the area-averaged magnetic field orientation and density structure orientation are perpendicular to each other at different scales in NGC 6334. This is because the global average statistics in Li et al. (2015) and the local statistics in our work trace different physics, i.e., while the global ordered magnetic field could guide gravitational collapse and lead to self-similar fragmentation (Li et al. 2015), the local field orientation can be distorted by gravity or affected by star formation activities.

4.3. Magnetic Field versus Local Gravity

The relative orientation between the magnetic field and local gravity ($\phi_B^{\rm LG}$) may indicate how effectively gravity can shape the magnetic field structure and how effectively the magnetic field can resist gravitational collapse (Koch et al. 2012a).

Figure 8 shows the RO–N relation for ϕ_B^{LG} from the Planck, JCMT, and ALMA observations. For the Planck observation, the magnetic field and local gravity change from a statistically slightly more perpendicular alignment (AM_B^{LG} $\lesssim 0$) to a slightly more parallel alignment (AM $_B^{LG} \gtrsim 0$), then change to a random alignment as $N_{\rm H_2}$ increases. Because the gravity is not expected to actively interact with the magnetic field in the diffuse region, the increasing AM-N trend at the lowest several $N_{\rm H_2}$ bins of the Planck data may be attributed to specific geometries where the direction of gravity coincidentally correlates with the complex-scale magnetic field in low-density regions within our direction-biased NANTEN2 ¹²CO (1-0) mask. For the JCMT observation toward the NGC 6334 filament, AM_B^{LG} is always positive and increases with $N_{\rm H_2}$, which indicates that gravity has an increasingly important role in shaping the magnetic field structure at higher densities. The similarity between the RO–N relations for $\phi_B^{\rm NG}$ and $\phi_B^{\rm LG}$ suggests that the direct reason for the transition from $AM_B^{\rm NG} < 0$ to $AM_B^{\rm NG} > 0$ (see Section 4.2 and Figure 7) may be related to the interplay between magnetic field and gravity. The statistically more parallel alignment between magnetic field, local gravity, and column density gradient at intermediate column densities probed by JCMT in NGC 6334 can be naturally explained by the scenario of a magnetized gravitational collapse (Mouschovias 1976a, 1976b). At even higher $N_{\rm H_2}$ bins revealed by ALMA observations toward individual clumps, the ${\rm AM}_B^{\rm LG}$ shows a prevailing decreasing trend with increasing $N_{\rm H_2}$ and transits back to ${\rm AM}_B^{\rm LG} \sim 0$ (in N6334I and IV) or even $AM_B^{LG} < 0$ (in N6334V) at the highest several N_{H_2} bins, except that the value of AM_B^{LG} in N6334I(N) stays positive across the $N_{\rm H_2}$ range. This may suggest that the magnetic field structure in high-density regions is not only shaped by gravity but also affected by star formation activities (e.g., converging flows, accretion, outflows, rotation, etc.). The distinct AM-N relations in different clumps may indicate their different star formation activities. For the ALMA observation, the magnetic field is better aligned with the local gravity than with the column density gradient (see Figures 7 and 8),

suggesting that ϕ_B^{LG} is better than ϕ_B^{NG} in studying the interaction between magnetic fields and gravity. The spatial distribution of ϕ_B^{LG} shows some patterns (see Appendix D), where local regions with small and large ϕ_B^{LG} values indicate weak and strong magnetic resistance against gravity (Koch et al. 2018), respectively. But more detailed analytical explanations for the spatial ϕ_B^{LG} distribution are yet to be established.

4.4. Velocity Gradient versus Magnetic Field

The relative orientation between velocity gradient and magnetic field (ϕ_{VG}^B) can be used as an indicator of the property of Alfvénic turbulence (Gonzalez-Casanova & Lazarian 2017; Lazarian & Yuen 2018; Lazarian et al. 2018), due to its intrinsic anisotropic nature (Goldreich & Sridhar 1995) in the absence of gravity. The degree of turbulence anisotropy increases as the Alfvénic Mach number decreases (i.e., stronger magnetic field and weaker turbulence).

Figure 9 shows the RO–N relation for ϕ_{VG}^{B} from the Planck, NANTEN2, JCMT, and ALMA observations. A clear trend is that the magnetic field and velocity gradient are statistically more perpendicular ($AM_{VG}^{B} < 0$) to each other at different column densities across several orders of magnitude. The more perpendicular alignment at low column densities is as expected from previous numerical studies and is consistent with previous observations (e.g., Yuen & Lazarian 2017a, 2017b; Gonzalez-Casanova & Lazarian 2017). However, the more perpendicular alignment at high column densities is different from previous numerical and observational studies, which have found that the magnetic field and velocity gradient transit to being statistically more parallel in high-density regions, due to the magnetized gravitational collapse (e.g., Yuen & Lazarian 2017a, 2017b; Tang et al. 2019). Note that the perpendicular alignment itself does not necessarily indicate sub-Alfvénic turbulence, because velocity anisotropy is also expected in super-Alfvénic turbulence at $< L_{\rm inj} M_{\rm A}^{-3}$ scales for a continuous turbulence cascade (Lazarian 2006), where $L_{\rm inj}$ is the turbulence injection scale and $M_{\rm A}$ is the Alfvénic Mach number. On the other hand, the statistical turbulence anisotropy level characterized by AM^B_{VG} does not vary too much at different scales (AM $_{VG}^{B}\sim -0.20$, -0.12, and -0.15 for Planck/NANTEN2, JCMT, and ALMA observations, respectively) despite a few outliers and some scatters, so we tentatively suggest that the average Alfvénic Mach number at each scale should be similar, i.e., the highdensity clumps/cores/condensations in NGC 6334 should also be trans-to-sub-Alfvénic because NGC 6334 is trans-to-sub-Alfvénic at complex/cloud scales (see discussions in Section 4.2). To our knowledge, our results may have provided some of the first observational evidence for a statistically more perpendicular local alignment between the magnetic field and velocity gradient in high-density regions with significant selfgravity. This suggests that, even if the magnetic field is distorted by gravity (see Section 4.3 and Appendix D) or impacted by star formation activities (see Sections 4.2 and 4.3), a strong magnetic field can still create anisotropic MHD turbulence locally. The trans-to-sub-Alfvénic state across scales of several orders of magnitude implies a significant role for the magnetic field in the star formation process in NGC 6334, which can explain the self-similar fragmentation at different scales as reported by Li et al. (2015). It should be noted that the trans-to-sub-Alfvénic state at clump/core/condensations scales in NGC 6334 does not conflict with the previous DCF

estimations (Liu et al. 2022a, 2022b; Pattle et al. 2022), because individual sources could still be sub-Alfvénic while the average state for a large sample of cloud substructures is transto-super-Alfvénic. On the other hand, the local magnetic field and velocity gradient are only weakly correlated (i.e., small $|AM_{VG}^B|$ values), so the local velocity gradient cannot be directly used as a tracer of the magnetic field orientation²¹ and the slightly anisotropic turbulence should not significantly affect the traditional DCF analysis, which requires an assumption of isotropic turbulence. The exact relation between the AM_{VG}^B and the Alfvénic Mach number is unclear and is worth future numerical studies.

4.5. Velocity Gradient versus Column Density Gradient

MHD turbulence can affect the scaling relation and anisotropy of the density structure (Cho & Lazarian 2003; Beresnyak et al. 2005; McKee & Ostriker 2007), where the column density gradient should be perpendicular to the magnetic field and parallel to the velocity gradient for sub-Alfvénic turbulence in the absence of gravity. Although several numerical studies have found that the line intensity gradient tends to be parallel to the subblock-averaged velocity gradient in self-gravitating regions (e.g., Yuen & Lazarian 2017a, 2017b), there is a lack of numerical studies on how the local velocity gradient and column density gradient should be correlated when gravity is significant.

Figure 10 shows the RO–N relation for ϕ_{VG}^{NG} from the Planck, NANTEN2, JCMT, and ALMA observations. The velocity gradient and column density gradient tend to be statistically slightly more parallel at lower column densities revealed by Planck and NANTEN2 observations, which agrees with the theoretical predictions for sub-Alfvénic turbulence. For JCMT and ALMA observations, there is no strong statistical relationship between the velocity gradient and column density gradient (AM $_{VG}^{NG} \sim 0$). We suggest that the local alignment between the two gradients does not provide too much information on the property of MHD turbulence or gravitational collapse in the self-gravitating region.

4.6. Velocity Gradient versus Local Gravity

It is expected that the gas motion will follow the direction of gravity during gravitational collapse. Thus, one may expect the velocity gradient to be aligned with the gravity direction.

Figure 11 shows the RO–N relation for ϕ_{VG}^{LG} from the Planck, NANTEN2, JCMT, and ALMA observations. No strong statistical relation is found between the local velocity gradient and gravity, except that the two angles tend to be slightly statistically more perpendicular to each other for the JCMT observation toward N6334I(N), where the reason for this perpendicular alignment is unclear. There could be several possible reasons for the general statistical uncorrelation between local velocity gradient and gravity: (1) despite there being large-scale velocity gradients in the NGC 6334 region across scales of several orders of magnitude (see Section 3.2), the small-scale local velocity gradient could be more reflective of the property of anisotropic MHD turbulence (see Section 4.4) instead of the large-scale ordered velocity field;

(2) the velocity gradient is just an approximation of the POS velocity and it does not perfectly trace the POS velocity; (3) several lines tend to be slightly optically thick (e.g., see Figure 5 and Arzoumanian et al. 2022) and do not trace the densest part of the gas that is more gravity-dominant; (4) the OCS and ¹³CS lines could be affected by specific star formation activities (shocks, outflows, rotation, etc.) and chemical processes in each clump. Thus, it is not surprising that the local velocity gradient and gravity are statistically not correlated with each other.

4.7. Normalized Mass-to-flux Ratio

Based on ideal MHD equations, Koch et al. (2012a) proposed that the local ratio between the magnetic field force (F_R) and the gravitational force (F_G) can be measured with

$$\Sigma_B = \frac{\sin \phi_{\text{LG}}^{\text{IG}}}{\sin(90^\circ - \phi_R^{\text{IG}})} = \frac{F_B}{|F_G|},\tag{6}$$

if the hydrostatic gas pressure is negligible, where "IG" stands for intensity gradient. Later, Koch et al. (2012b) further suggested that the mass-to-flux ratio normalized to the critical value within a specific region is given by

$$\lambda_{\text{KTH}} = \langle \Sigma_R^{-1/2} \rangle \pi^{-1/2},\tag{7}$$

where $\lambda_{\rm KTH} > 1$ indicates that gravity dominates the magnetic field (i.e., magnetically supercritical) and vice versa. We calculate $\lambda_{\rm KTH}$ at different $N_{\rm H_2}$ bins. The basic assumption of the KTH method is that the dust emission intensity gradient traces the transport of matter as a result of the MHD force equation. Because the matter distribution is reflected by the column density map rather than the dust intensity map, we use the column density gradient instead of the intensity gradient in the calculation.

Figure 12 shows λ_{KTH} as a function of N_{H} , from the Planck, JCMT, and ALMA observations. For the majority of Planck observations, there is $\lambda_{\text{KTH}} < 1$. Only at the highest N_{H_2} bin do we see $\lambda_{KTH} \sim 1$. For the JCMT observation of the whole NGC 6334 filament, the λ_{KTH} increases with increasing N_{H_2} and transits from $\lambda_{\rm KTH} < 1$ to $\lambda_{\rm KTH} > 1$. The ALMA observations toward individual clumps show similar trends of increasing λ_{KTH} with N_{H_2} . It should be noted that the magnetic field could be affected by star formation feedback (e.g., outflow, H II regions, etc.) in the vicinity of young stellar objects at high column densities revealed by ALMA, which can violate the assumption of the KTH method and make the estimated λ_{KTH} unreliable. If we only look at the Planck and JCMT observations, the prevailing increasing trend of λ_{KTH} with $N_{\rm H_2}$ is consistent with previous DCF estimations (Liu et al. 2022a, 2022b). Assuming uncertainties of a factor of 2 for both λ_{KTH} and N_{H_2} , we perform a simple least-squares fit for the power-law relation between λ_{KTH} and N_{H_2} for the JCMT observation. We obtain $\lambda \propto N^{0.10}$, which transfers to the relation between the magnetic field and column density as $B \propto N^{0.90}$, adopting $\lambda \propto N/B$ (e.g., Crutcher et al. 2004). The power-law index of 0.90 for the B-N relation is larger than the value of 0.72 previously reported for the compilation of DCF estimations (Liu et al. 2022a). Note that the uncertainty of the $\lambda_{\rm KTH}$ estimated from the KTH method is unknown due to the lack of direct numerical tests. Moreover, the uncertainty on the absolute column density of the Planck observation and JCMT

²¹ It should be noted that our approach in the comparison between the magnetic field and velocity gradient is different from that of the VGT, which requires subblock-averaging (Yuen & Lazarian 2017a, 2017b) for the velocity gradient. Thus, our results are not contrary to the validity of the VGT.

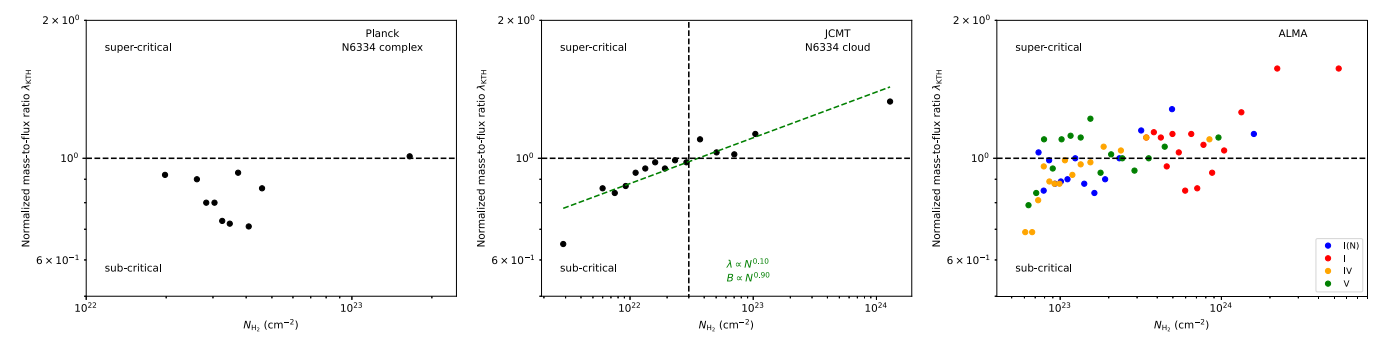


Figure 12. Normalized mass-to-flux ratio derived from the KTH method as a function of column density for Planck (left), JCMT (middle), and ALMA (right) observations. The JCMT observation filters out the large-scale emission corresponding to $N_{\rm H_2} \sim 3 \times 10^{22}$ cm⁻² (Arzoumanian et al. 2021), which is indicated by the vertical dashed line. The ALMA observation filters out the large-scale emission at scales >0.08 pc. The highest $N_{\rm H_2}$ bin of Planck observations contains the area of the NGC 6334 filament covered by the JCMT observation. The highest $N_{\rm H_2}$ bin of JCMT observations contains the area of the N6334I(N), I, IV, and V covered by the ALMA observation. The absolute column densities from different instruments are not comparable. Planck, JCMT, and ALMA observations trace low, intermediate, and high column densities, respectively.

observation (in the extended region) is also unclear (see Appendix C). Thus, we stop at discussions of the $\lambda_{\rm KTH}-N_{\rm H_2}$ trend and refrain from determining the transition column density for $\lambda_{\rm KTH}\sim 1$.

5. Summary

With ALMA dust polarization and molecular line observations toward four massive clumps (NGC6334I(N), I, IV, and V) in the massive star-forming region NGC 6334, in conjunction with the large-scale dust polarization and molecular line data from Planck, NANTEN2, and JCMT, we reveal the relative orientations between magnetic fields, gas column density gradients, local gravity, and velocity gradients, and we study their varying trend with column density in NGC 6334. We suggest that a synergistic study of local relative orientations between different angles is powerful at revealing the physical condition of molecular clouds at different scales. The major findings and conclusions are:

- 1. The column density gradient and local gravity do not have a preferred relative orientation in the diffuse region surrounding the NGC 6334 filament, suggesting that the density structure of the low-density region is not significantly affected by gravity. Within the NGC 6334 filament, the two angles are closely aligned with each other, suggesting that gravity has an important role in shaping the density structure in self-gravitating star formation clouds.
- 2. As the column density increases, the alignment between magnetic fields and column density gradients transits from statistically more perpendicular to parallel, which agrees with trans-to-sub-Alfvénic simulations of previous numerical studies and suggests NGC 6334 is trans-tosub-Alfvénic at complex/cloud scale. At low column densities, the more perpendicular alignment may be due to the interaction between magnetic fields and turbulence. At intermediate column densities, the alignment between magnetic fields and local gravity shows a density-varying trend similar to the relative orientation between magnetic fields and column density gradients, which suggests the magnetic field is entrained by gravity and the statistically more parallel alignment between magnetic fields and column density gradients is most likely due to a magnetized gravitational collapse. At even higher column densities, the magnetic field and column density

gradient/local gravity transits back to having no preferred orientation or being statistically slightly more perpendicular, which may suggest the magnetic field structure is impacted by star formation activities. Our results in conjunction with the results in Li et al. (2015) suggest that the magnetic field can guide gravitational collapse and self-similar fragmentation globally but is distorted by gravity and affected by star formation activities locally.

- 3. The local velocity gradient tends to be statistically more perpendicular to the local magnetic field orientation across our considered spatial scales. The degree of alignment does not change too much at different column densities, which may suggest that the NGC 6334 region remains trans-to-sub-Alfvénic at small scales. This signifies an important role of magnetic fields in the star formation process in NGC 6334, despite it being dragged by gravity and impacted by star formation activities in intermediate- to high-density regions.
- 4. No clear general statistical relation is found between the velocity gradient and column density gradient/local gravity.
- 5. The normalized mass-to-flux ratio derived from the KTH method tends to increase with column density, which agrees with previous DCF estimations. But the KTH method may fail at high column densities, due to the breakdown of the underlying assumptions.

We thank the anonymous referee for the constructive comments. We thank Dr. Doris Arzoumanian for sharing the JCMT dust polarization maps and the Herschel temperature maps. We thank Dr. Yasuo Fukui and Dr. Mikito Kohno for sharing the NANTEN2 data. J.L. thanks Dr. Daniel Seifried for helpful comments.

J.L. acknowledges the support from the EAO Fellowship Program under the umbrella of the East Asia Core Observatories Association. K.Q. is supported by National Key R&D Program of China grant No. 2022YFA1603100. K.Q. acknowledges the support from National Natural Science Foundation of China (NSFC) through grant Nos. U1731237, 11590781, and 11629302. H.B.L. is supported by the Ministry of Science and Technology (MoST) of Taiwan (grant Nos. 108-2112-M-001-002-MY3, 108-2923-M-001-006-MY3, 111-2112-M-001-089-MY3). Z.Y.L is supported in part by NSF AST-1815784 and NASA 20NSSC18K1095. This work was also partially supported by the program Unidad de Excelencia Maria de Maeztu CEX2020-

001058-M. J.M.G also acknowledges support by the grant PID2020-117710GB-I00 (MCI-AEI-FEDER, UE).

This paper makes use of the following ALMA data: ADS/ JAO.ALMA#2017.1.00793.S. ALMA is a partnership of the ESO (representing its member states), NSF (USA) and NINS (Japan), together with NRC (Canada), MOST and ASIAA (Taiwan), and KASI (Republic of Korea), in cooperation with the Republic of Chile. The Joint ALMA Observatory is operated by ESO, auI/NRAO, and NAOJ. The National Radio Astronomy Observatory is a facility of the National Science Foundation operated under cooperative agreement by Associated Universities, Inc. The JCMT is operated by the EAO on behalf of NAOJ, ASIAA, KASI, and CAMS, as well as the National Key R&D Program of China (No. YFA0402700). Additional funding support is provided by the STFC and participating universities in the UK and Canada. Additional funds for the construction of SCUBA-2 were provided by the Canada Foundation for Innovation. This work is based on observations obtained with Planck (http://www. esa.int/Planck), an ESA science mission with instruments and contributions directly funded by ESA Member States, NASA, and Canada. The present study has also made use of NANTEN2 data. NANTEN2 is an international collaboration of ten universities: Nagoya University, Osaka Prefecture University, University of Cologne, University of Bonn, Seoul

National University, University of Chile, University of New South Wales, Macquarie University, University of Sydney, and Zurich Technical University.

Facilities: Planck(HFI), NANTEN2, JCMT(HARP, SCUBA-2, POL-2), ALMA.

Software; Astropy (Astropy Collaboration et al. 2013, 2018), Matplotlib (Hunter 2007).

Appendix A Integrated Line Intensity Maps

Figures 13 and 14 present the integrated intensity (moment 0) maps of the NANTEN2 12 CO (1–0), JCMT 13 CO (3–2), and ALMA OCS and 13 CS data. The integrated intensity at position x is calculated with $\sum_{i}^{N_{\rm ch}}I_{i}(x)\Delta\nu_{\rm ch}$. The propagated uncertainty of the integrated intensity is given by $\sqrt{N_{\rm ch}}\sigma_{\rm ch}\Delta\nu_{\rm ch}$ (e.g., Caselli et al. 2002; Teague 2019). Following Arzoumanian et al. (2022), the large-scale NANTEN2 12 CO (1–0) and JCMT 13 CO (3–2) lines are integrated from -12 to 4 km s $^{-1}$. The ALMA OCS and 13 CS are integrated within slightly different velocity ranges, as indicated in Figure 14. In general, the integrated line emissions agree with the dust continuum emission near the emission peaks, but they show some differences in extended regions.

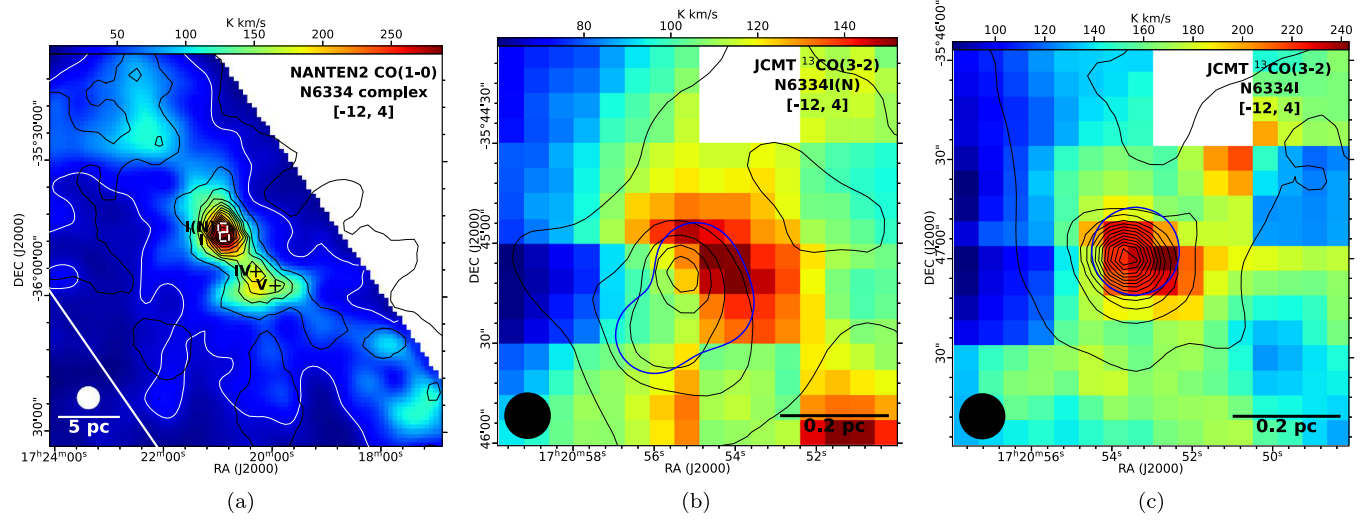


Figure 13. (a). Moment 0 map (colorscale) of NANTEN2 12 CO (1–0) line emission toward NGC 6334 complex (Fukui et al. 2018) from -12 to 4 km s $^{-1}$. The line data are convolved to a beam size of 5′. The black contour levels correspond to the Planck $τ_{353}$ map. Contour starts at 0.0004 and continues with an interval of 0.0004. The white rectangles indicate the map area of the JCMT fields toward N6334I(N) and I in (b) and (c). Black crosses indicate the positions of N6334IV and V. The white contour indicates the region with NANTEN2 integrated 12 CO (1–0) intensity greater than 25 K km s $^{-1}$ within which we perform the relative orientation analysis. (b)–(c). Moment 0 maps (colorscale) of JCMT 13 CO (3–2) line emission from -12 to 4 km s $^{-1}$ toward N6334I(N) and N6334I. The black contour levels correspond to the JCMT 850 μm dust continuum map. Contour starts at 2 Jy beam $^{-1}$ and continues with an interval of 4 Jy beam $^{-1}$. Blue contours show the FWHM field of view of our ALMA observations.

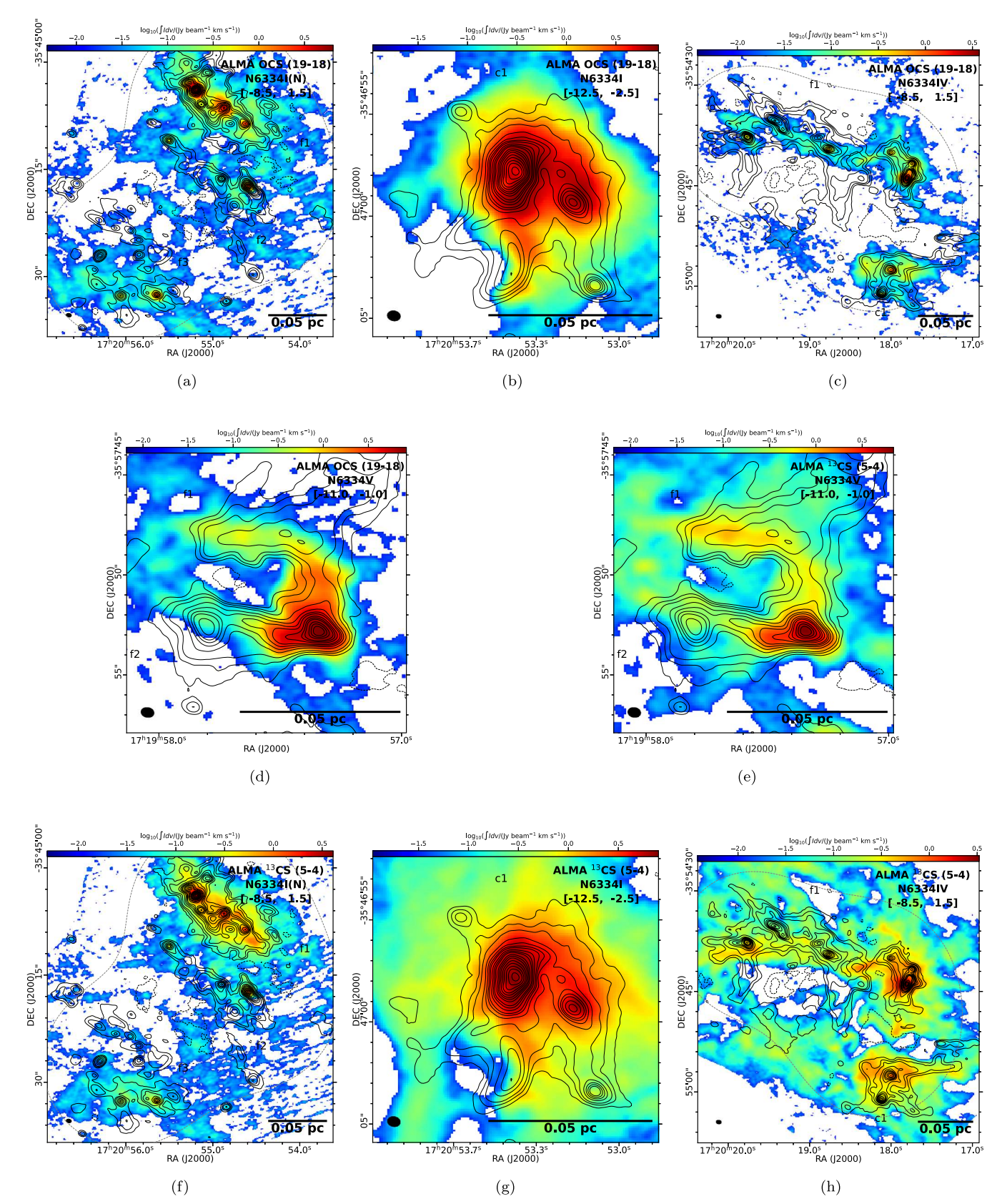


Figure 14. Moment 0 maps (colorscale) of ALMA OCS ((a)–(d)) and 13 CS ((e)–(h)) observations. The black contour levels correspond to the ALMA dust continuum map. Contour levels are (± 3 , 6, 10, 20, 30, 40, 50, 70, 90, 110, 150, 180, 210, 250, 290, 340, 390, 450) $\times \sigma_I$. Gray dashed contours indicate the FWHM field of view of the ALMA observations.

Appendix B Uncertainties

B.1. Uncertainty of the Gradient Orientation

The column density gradient is calculated with (Planck Collaboration et al. 2016)

$$\nabla N = (G_x \circledast N)\hat{i} + (G_y \circledast N)\hat{j} = g_y \hat{i} + g_y \hat{j}, \qquad (B1)$$

where G_x and G_y are the x- and y-derivatives of the Sobel kernel. The orientation of ∇N is given by $\theta_{NG} = \arctan(-g_x, g_y)$. The uncertainty of the column density gradient is given by Planck Collaboration et al. (2016)

$$\nabla \delta N = (G_x \otimes \delta N)\hat{i} + (G_y \otimes \delta N)\hat{j} = \delta_{gx}\hat{i} + \delta_{gy}\hat{j}, \quad (B2)$$

where δN is the uncertainty of the column density. The uncertainty of θ_{NG} is given by Planck Collaboration et al. (2016)

$$\delta\theta_{\rm NG} = \frac{1}{g_x^2 + g_y^2} \sqrt{g_y^2 \sigma_{gx}^2 + g_x^2 \sigma_{gy}^2},$$
 (B3)

where σ_{gx} and σ_{gy} are the rms of δ_{gx} and δ_{gy} . In our case, we calculate σ_{gx} and σ_{gy} within the 3 × 3 box. The velocity centroid gradient and its uncertainty can be calculated similarly.

B.2. Uncertainty of the Alignment Measure Parameter AM

The uncertainty of $AM = \langle \cos(2\phi) \rangle$ comes from the standard error on the mean and the propagation of the observational uncertainty.

For a statistically independent sample of n' observations toward f (in our case $f = \cos(2\phi)$), we have

$$STD(f) = \sqrt{RMS(f)^2 - \langle f \rangle^2}, \qquad (B4)$$

where STD(f) is the standard deviation of f. The relation between the statistical standard error of $\langle f \rangle$ (i.e., $\delta \langle f \rangle_{\text{stat}}$) and the standard deviation of f is

$$\delta \langle f \rangle_{\text{stat}} = \frac{1}{n'} \text{STD}(f).$$
 (B5)

Thus, the uncertainty of AM from the statistical error on the mean is given by

$$\delta AM_{\text{stat}} = \delta \langle f \rangle_{\text{stat}} = \sqrt{(\langle (\cos{(2\phi)})^2 \rangle - AM^2)/n'}$$
. (B6)

On the other hand, the propagated observational uncertainty of $f = \cos(2\phi)$ is

$$\delta f_{\rm obs} \sim |2\sin(2\phi)\delta\phi|.$$
 (B7)

For $\langle f \rangle$, the propagated observational uncertainty is

$$\delta \langle f \rangle_{\text{obs}} = \text{RMS}(\delta f_{\text{obs}}).$$
 (B8)

Thus, the propagated observational uncertainty of AM is given by

$$\delta AM_{\text{obs}} = \delta \langle f \rangle_{\text{obs}} = \sqrt{(\sum_{i}^{n'} (2\sin(2\phi_{i})\delta\phi_{i})^{2})/n'}$$
. (B9)

Finally, the combined uncertainty of AM is given by

$$\delta AM = \sqrt{\delta AM_{\text{stat}}^2 + \delta AM_{\text{obs}}^2}.$$
 (B10)

Appendix C Temperature and Column Density

We use multi-transition CH₃OH lines from ALMA observations to derive the physical conditions near the young stellar objects. Table 3 lists the information of these CH₃OH lines from the CDMS²² catalog. We perform a simple rotation diagram analysis (Goldsmith & Langer 1999) with the CH₃OH lines to estimate the gas temperature under the assumptions of local thermal equilibrium and optically thin. The upper state level population of CH₃OH is given by

$$N_{\rm u} = \frac{N_{\rm CH_3OH}}{Z} g_{\rm u} e^{-E_{\rm u}/kT_{\rm rot}},\tag{C1}$$

where N_u is the column density of the upper state, $N_{\text{CH}_3\text{OH}}$ is the total column density of CH₃OH, g_u is the statistical weight of the upper state, E_u is the upper energy level, k is the Boltzmann constant, T_{rot} is the rotation temperature, and Z is the partition function. We fit the rotation diagram of the four transitions of CH₃OH to derive the rotation temperature of each pixel. If the transition with the highest E_{up} (i.e., ~ 508 K) is not detected, we only fit the other three transitions. If the transition with $E_{\text{up}} \sim 190$ K is not detected, we do not fit the rotation diagram. Figure 15 shows the rotation temperature maps of the four clumps. A general trend is that the T_{rot} decreases from hundreds of Kelvins near dust emission peaks to less than 100 K in extended regions. The peak temperatures in N6334I(N), I, IV, and V are ~ 220 , 400, 250, and 220 K, respectively, suggesting a ubiquity of hot cores in the massive clumps in NGC 6334.

Assuming optically thin dust emission, the dust mass can be estimated as

$$M_{\text{dust}} = \frac{F_{\nu} d^2}{\kappa_{\nu} B_{\nu}(T)},\tag{C2}$$

where F_{ν} is the flux density at frequency ν , d is the distance, $\kappa_{\nu} = (\nu/1\text{THz})^{\beta}$ is the dust opacity (Hildebrand 1983) in m² kg⁻¹, and $B_{\nu}(T)$ is the Planck function at temperature T. Previous multiwavelength dust emission observations toward massive star-forming regions have found dust emissivity indexes (β) of \sim 1.5 (e.g., Beuther et al. 2007; Chen et al. 2007). Adopting $\beta = 1.5$, the κ_{ν} is estimated to be 0.10 m² kg⁻¹ at $\nu \sim$ 220 GHz. We adopt the rotation temperature derived from the rotation diagram analysis as the dust temperature. For regions without $T_{\rm rot}$

Table 3
Summary of CH₃OH Lines

Frequency (GHz)	Transition	g _u ^a	E _u b (K)	$\frac{A_{\rm ul}^{\ c}}{((10^{-5}{\rm s}^{-1}))}$
216.945521	5 ₁ -4 ₂ E	44	55.87116	1.21
217.886504	$20_1 - 20_0 E$	164	508.37554	3.38
218.440063	$4_{2}-3_{1}E$	36	45.45944	4.69
232.945797	10_{-3} - 11_{-2} E	84	190.36958	2.13

Notes.

^a Statistical weight of the upper state.

^c Einstein A coefficient.

^b Upper energy level.

²² https://cdms.astro.uni-koeln.de/

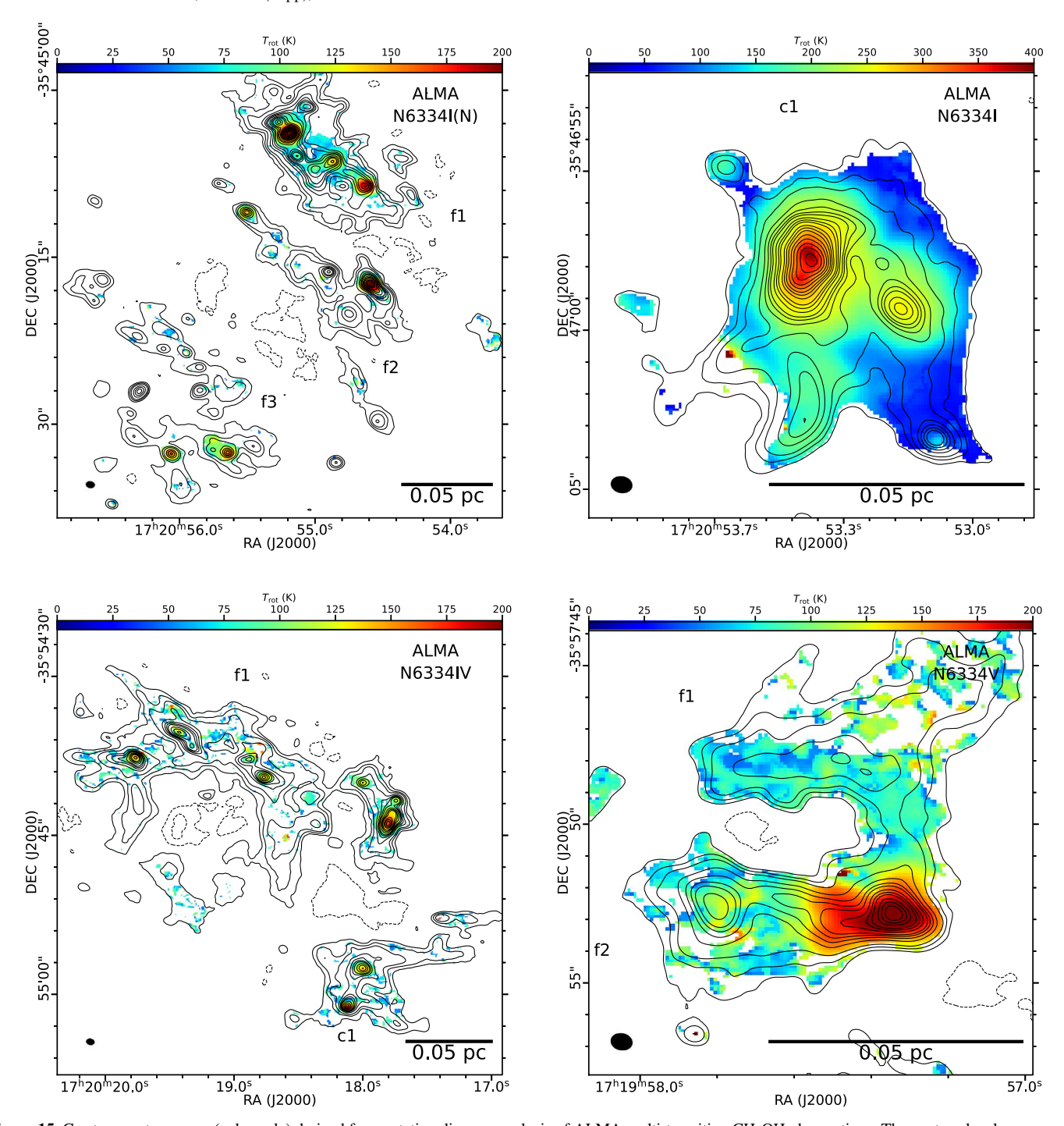


Figure 15. Gas temperature maps (colorscale) derived from rotation diagram analysis of ALMA multi-transition CH₃OH observations. The contour levels correspond to the ALMA dust continuum map. Contour levels are (± 3 , 6, 10, 20, 30, 40, 50, 70, 90, 110, 150, 180, 210, 250, 290, 340, 390, 450) $\times \sigma_I$.

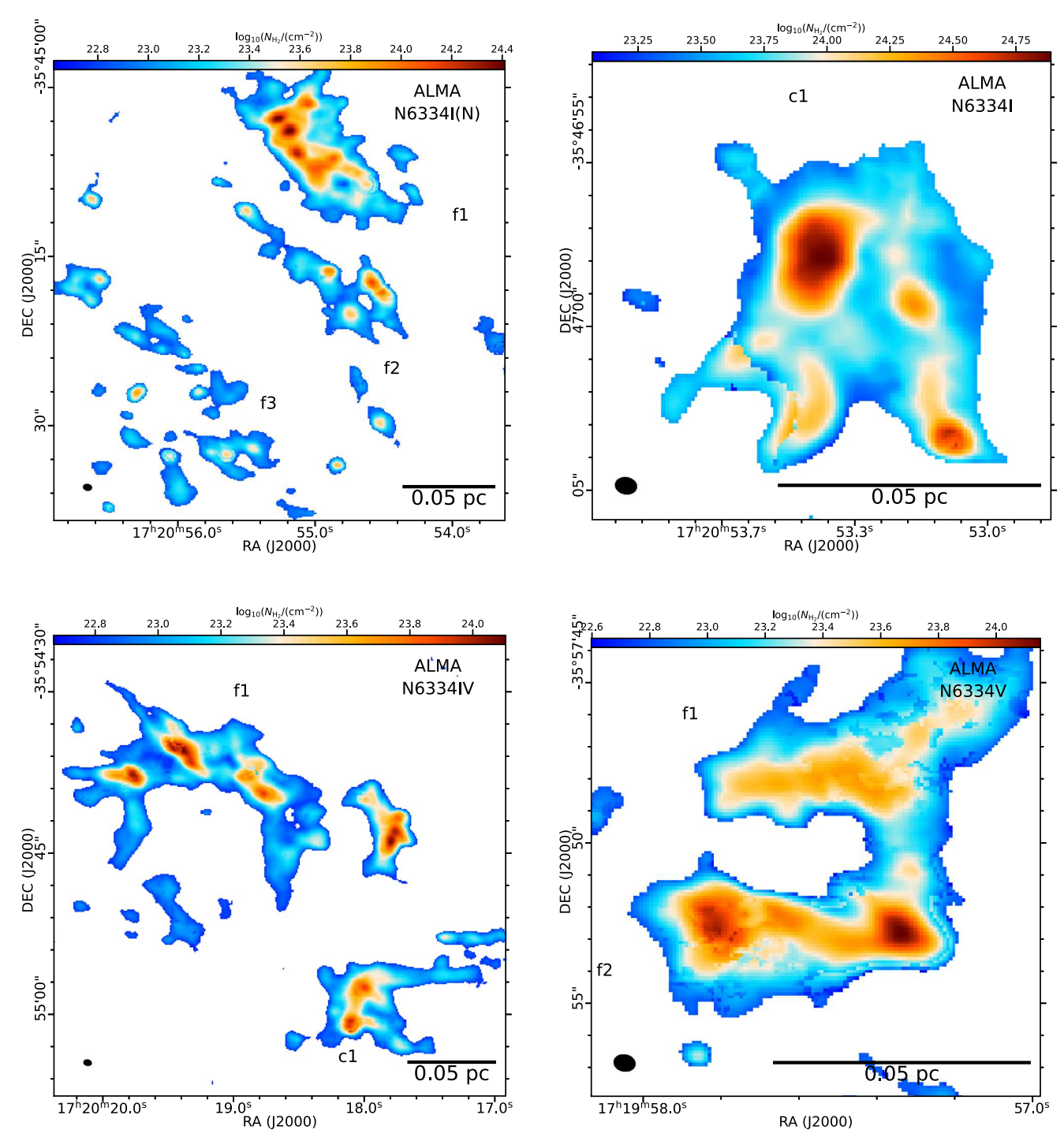


Figure 16. Column density maps (colorscale) derived from ALMA dust emission observations.

estimation, we adopt T=80 K, which is approximately the most common temperature in extended regions (see Figure 15). Adopting a gas-to-dust ratio of $\Lambda=100$ (Savage & Jenkins 1972), the gas mass is estimated with $M_{\rm gas}=\Lambda M_{\rm dust}$. The gas column

density is then estimated with

$$N_{\rm H_2} = \frac{M_{\rm gas}}{\mu_{\rm H_2} m_{\rm H} A},$$
 (C3)

where $\mu_{\rm H_2} = 2.8$ is the mean molecular weight per hydrogen molecule (Kauffmann et al. 2008), $m_{\rm H}$ is the atomic mass of hydrogen, and A is the area. Figure 16 shows the column density maps of the four clumps.

For the JCMT observations from BISTRO, we estimate the gas mass and column density from the Stokes I map of dust emission with Equations (C2) and (C3), but we adopt a constant temperature T=20 K (Arzoumanian et al. 2021) and $\kappa_{\nu}=0.21$ m² kg⁻¹ (at $\nu\sim353$ GHz). Arzoumanian et al. (2021) found that the JCMT observations of NGC 6334 filters out the large-scale emission on the order of $N_{\rm H_2}=3\times10^{22}$ cm⁻².

For the Planck observations, we scale the dust optical depth (τ_{353}) map to atomic hydrogen column density $(N_{\rm H})$ map with the relation (Planck Collaboration et al. 2014)

$$\tau_{353}/N_{\rm H} = 1.2 \times 10^{-26} {\rm cm}^2$$
. (C4)

The variation of the $\tau_{353}/N_{\rm H}$ ratio can be more than a factor of 2 from diffuse to dense ISM, but the statistics of relative orientation does not critically depend on this calibration (Planck Collaboration et al. 2016). We convert $N_{\rm H}$ to $N_{\rm H_2}$ with the relation $N_{\rm H}=2N_{\rm H_2}$.

Appendix D Relative Orientation between Magnetic Field and Local Gravity

The angle $\phi_B^{\rm LG}=|\theta_B-\theta_{\rm LG}|$ characterizes the relative orientation between magnetic fields and local gravity. Figures 17 and 18 show the $\phi_B^{\rm LG}$ maps from Planck, JCMT, and ALMA observations. The spatial distribution of $\phi_B^{\rm LG}$ is not random. At different scales, a common pattern is a tangential fanlike distribution of $\phi_B^{\rm LG}$ with low and high values appearing alternately near the emission peaks, which may suggest the gravitational infall/collapse can occur locally through the magnetic channels with small $\phi_B^{\rm LG}$ values (Koch et al. 2018). The $\phi_B^{\rm LG}$ distribution is clear in some regions, e.g., small and large $\phi_B^{\rm LG}$ values are found in the main part and ends of N6334I(N)-f1, respectively, which agrees with the scenario of a magnetized gravitational collapse and clearly suggests the magnetic field structure is shaped by gravity in the main part and is being distorted by gravity in the ends. However, the $\phi_B^{\rm LG}$ distribution is complex in most regions. Although Koch et al. (2012a) and Koch et al. (2018) have suggested that small and large $\phi_B^{\rm LG}$ (or ω in their work) values indicate weak and strong magnetic resistance against gravity, respectively, more detailed analytical explanations of

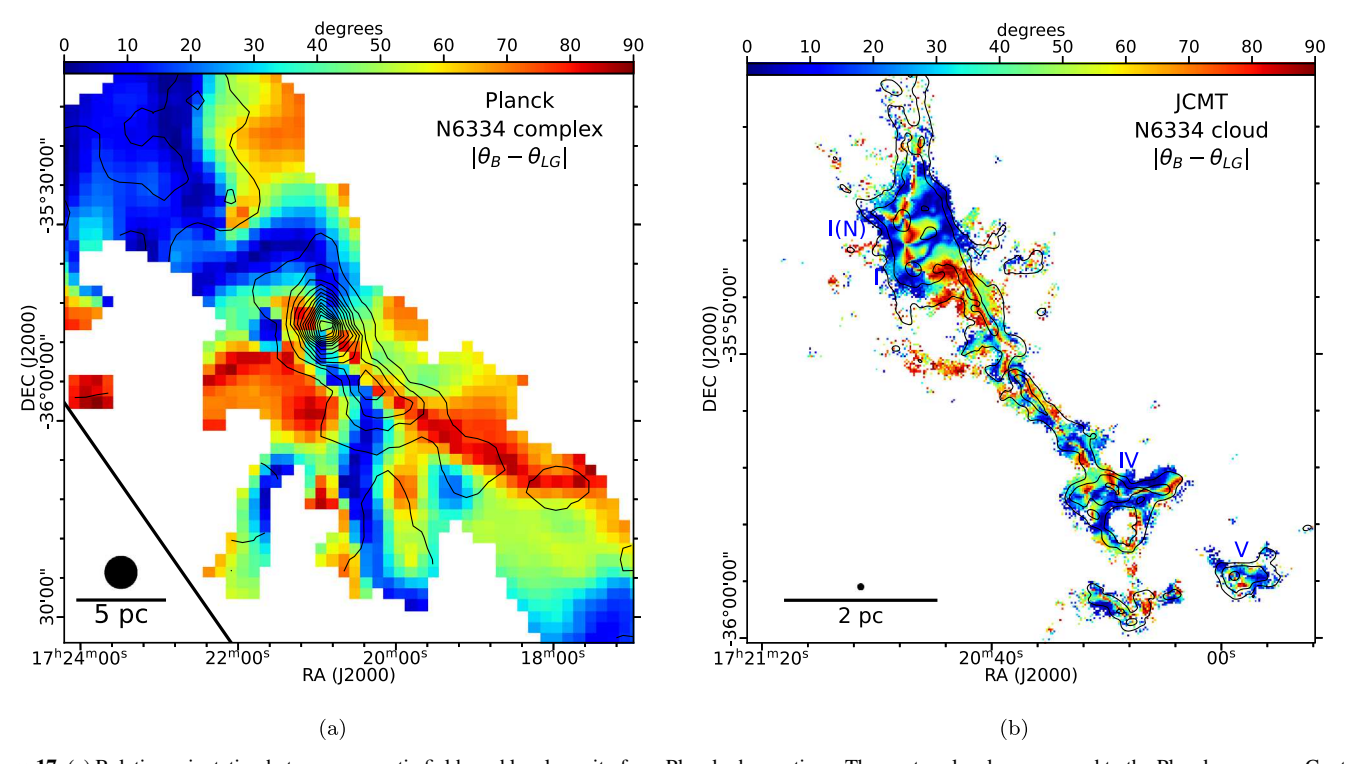


Figure 17. (a) Relative orientation between magnetic fields and local gravity from Planck observations. The contour levels correspond to the Planck au_{353} map. Contour starts at 0.0004 and continues with an interval of 0.0004. Only data points with NANTEN2 integrated ^{12}CO (1–0) intensity greater than 25 K km s⁻¹ are shown. (b) Relative orientation between magnetic fields and local gravity from JCMT observations. Values of ϕ_B^{LG} at positions with S/N(PI)>3 are shown. The contour levels correspond to the JCMT 850 μ m dust continuum map. Contour starts at 2 Jy beam⁻¹ and continues with an interval of 4 Jy beam⁻¹.

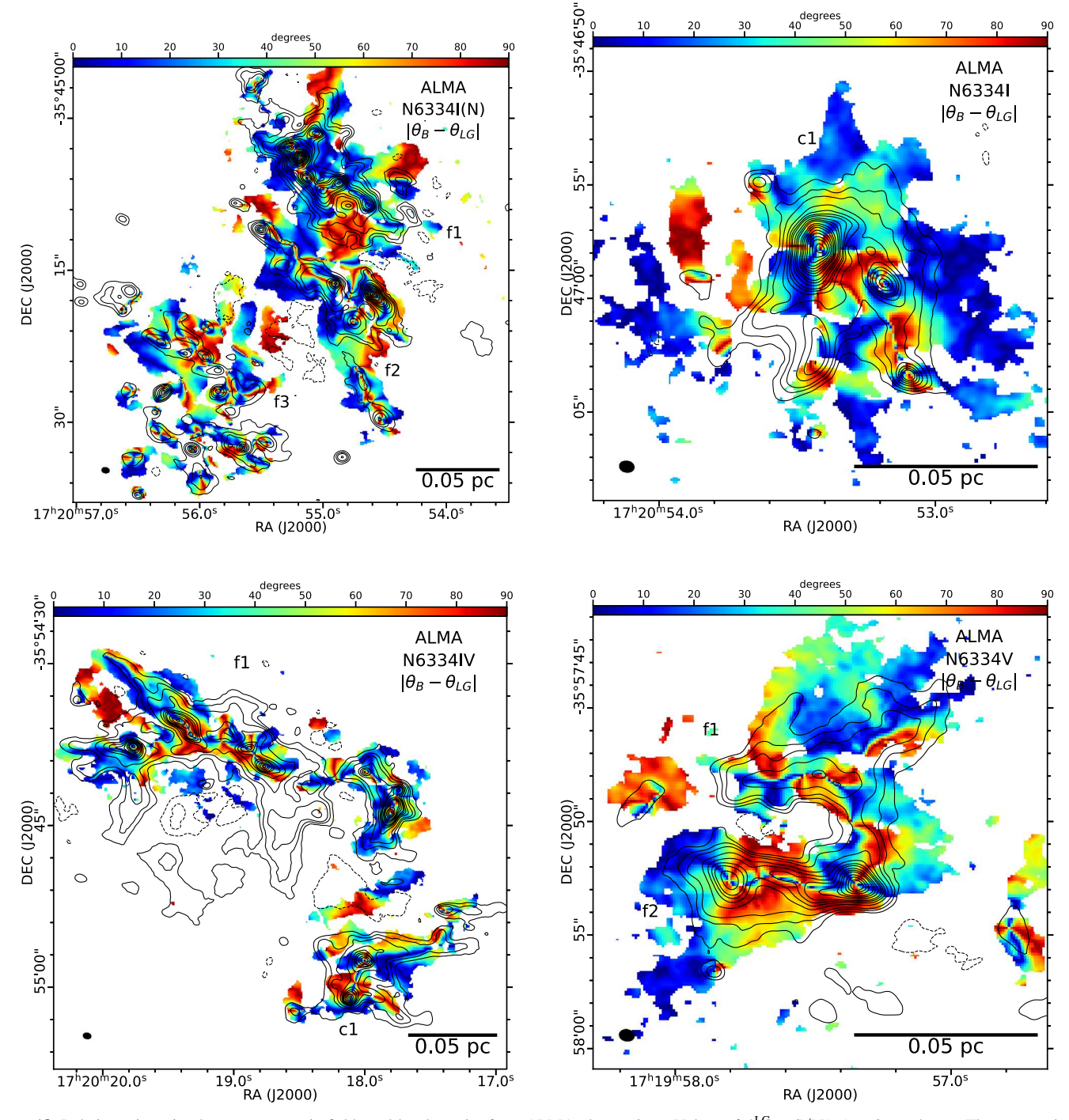


Figure 18. Relative orientation between magnetic fields and local gravity from ALMA observations. Values of ϕ_B^{LG} at S/N(PI) > 2 are shown. The contour levels correspond to the ALMA dust continuum map. Contour levels are (±3, 6, 10, 20, 30, 40, 50, 70, 90, 110, 150, 180, 210, 250, 290, 340, 390, 450) $\times \sigma_I$.

different spatial $\phi_B^{\rm LG}$ distributions are yet to be established. The local variation for the spatial distribution of other relative orientations ($\phi_{NG}^{\rm LG}$, $\phi_B^{\rm NG}$, $\phi_{VG}^{\rm NG}$, $\phi_{VG}^{\rm NG}$, and $\phi_{VG}^{\rm LG}$) are less clear than that of $\phi_B^{\rm LG}$, and thus we do not shown them in this paper.

ORCID iDs

Junhao Liu (刘峻豪) ® https://orcid.org/0000-0002-4774-2998 Qizhou Zhang ® https://orcid.org/0000-0003-2384-6589 Patrick M. Koch ® https://orcid.org/0000-0003-2777-5861 Hauyu Baobab Liu ® https://orcid.org/0000-0003-2300-2626 Zhi-Yun Li https://orcid.org/0000-0002-7402-6487 Shanghuo Li https://orcid.org/0000-0003-1275-5251 Josep Miquel Girart https://orcid.org/0000-0002-3829-5591 Huei-Ru Vivien Chen https://orcid.org/0000-0002-9774-1846 Tao-Chung Ching https://orcid.org/0000-0001-8516-2532

Tao-Chung Ching https://orcid.org/0000-0001-8516-253
Paul T. P. Ho https://orcid.org/0000-0002-3412-4306
Shih-Ping Lai https://orcid.org/0000-0001-5522-486X
Keping Qiu https://orcid.org/0000-0002-5093-5088
Ramprasad Rao https://orcid.org/0000-0002-1407-7944
Ya-wen Tang https://orcid.org/0000-0002-0675-276X

References

```
Añez-López, N., Busquet, G., Koch, P. M., et al. 2020, A&A, 644, A52
Andersson, B.-G., Lazarian, A., & Vaillancourt, J. E. 2015, ARA&A, 53, 501
Andre, P., Reveret, V., Konyves, V., et al. 2016, A&A, 592, A54
Arzoumanian, D., Furuya, R. S., Hasegawa, T., et al. 2021, A&A, 647, A78
Arzoumanian, D., Russeil, D., Zavagno, A., et al. 2022, A&A, 660, A56
Astropy Collaboration, Robitaille, T. P., Tollerud, E. J., et al. 2013, A&A,
  558. A33
Astropy Collaboration, Price-Whelan, A. M., Sipőcz, B. M., et al. 2018, AJ,
  156, 123
Beresnyak, A., Lazarian, A., & Cho, J. 2005, ApJL, 624, L93
Beuther, H., Leurini, S., Schilke, P., et al. 2007, A&A, 466, 1065
Beuther, H., Soler, J. D., Linz, H., et al. 2020, ApJ, 904, 168
Buckle, J. V., Hills, R. E., Smith, H., et al. 2009, MNRAS, 399, 1026
Caselli, P., Benson, P. J., Myers, P. C., & Tafalla, M. 2002, ApJ, 572, 238
Chandrasekhar, S., & Fermi, E. 1953, ApJ, 118, 113
Chen, C.-Y., King, P. K., & Li, Z.-Y. 2016, ApJ, 829, 84
Chen, H.-R., Su, Y.-N., Liu, S.-Y., et al. 2007, ApJL, 654, L87
Cheung, L., Frogel, J. A., Gezari, D. Y., & Hauser, M. G. 1978, ApJL,
   226, L149
Chibueze, J. O., Omodaka, T., Handa, T., et al. 2014, ApJ, 784, 114
Cho, J., & Lazarian, A. 2003, MNRAS, 345, 325
Corradi, R. L. M., Aznar, R., & Mampaso, A. 1998, MNRAS, 297, 617
Cortes, P. C., Sanhueza, P., Houde, M., et al. 2021, ApJ, 923, 204
Crutcher, R. M. 2012, ARA&A, 50, 29
Crutcher, R. M., Nutter, D. J., Ward-Thompson, D., & Kirk, J. M. 2004, ApJ,
Currie, M. J., Berry, D. S., Jenness, T., et al. 2014, in ASP Conf. Ser. 485,
   Astronomical Data Analysis Software and Systems XXIII, ed. N. Manset &
   P. Forshay (San Francisco, CA: ASP), 391
Davis, L. 1951, PhRv, 81, 890
Davis, L., & Greenstein, J. L. 1949, PhRv, 75, 1605
Dickman, R. L., & Kleiner, S. C. 1985, ApJ, 295, 479
Friberg, P., Bastien, P., Berry, D., et al. 2016, Proc. SPIE, 9914, 991403
Fukui, Y., Kohno, M., Yokoyama, K., et al. 2018, PASJ, 70, S41
Gezari, D. Y. 1982, ApJL, 259, L29
Girart, J. M., Frau, P., Zhang, Q., et al. 2013, ApJ, 772, 69
Girart, J. M., Fernandez-Lopez, M., Li, Z.-Y., et al. 2018, ApJL, 856, L27
Girichidis, P. 2021, MNRAS, 507, 5641
Goldreich, P., & Sridhar, S. 1995, ApJ, 438, 763
Goldsmith, P. F., & Langer, W. D. 1999, ApJ, 517, 209
Gonzalez-Casanova, D. F., & Lazarian, A. 2017, ApJ, 835, 41
Hildebrand, R. H. 1983, QJRAS, 24, 267
Holland, W. S., Bintley, D., Chapin, E. L., et al. 2013, MNRAS, 430, 2513
Hu, Y., Yuen, K. H., Lazarian, V., et al. 2019, NatAs, 3, 776
Hull, C. L. H., & Zhang, Q. 2019, FrASS, 6, 3
Hunter, J. D. 2007, CSE, 9, 90
Juarez, C., Girart, J. M., Zamora-Aviles, M., et al. 2017, ApJ, 844, 44
Kauffmann, J., Bertoldi, F., Bourke, T. L., Evans, N. J., & Lee, C. W. 2008,
    &A, 487, 993
Koch, P. M., Tang, Y.-W., & Ho, P. T. P. 2012a, ApJ, 747, 79
Koch, P. M., Tang, Y.-W., & Ho, P. T. P. 2012b, ApJ, 747, 80
Koch, P. M., Tang, Y.-W., Ho, P. T. P., et al. 2018, ApJ, 855, 39
```

Kwon, W., Pattle, K., Sadavoy, S., et al. 2022, ApJ, 926, 163

```
Lamarre, J.-M., Puget, J.-L., Ade, P. A. R., et al. 2010, A&A, 520, A9
Lazarian, A. 2006, ApJL, 645, L25
Lazarian, A. 2007, JQSRT, 106, 225
Lazarian, A., & Hoang, T. 2007, MNRAS, 378, 910
Lazarian, A., & Yuen, K. H. 2018, ApJ, 853, 96
Lazarian, A., Yuen, K. H., Ho, K. W., et al. 2018, ApJ, 865, 46
Lazarian, A., Yuen, K. H., & Pogosyan, D. 2022, ApJ, 935, 77
Li, H.-b., Yuen, K. H., Otto, F., et al. 2015, Natur, 520, 518
Liu, H. B. 2021, ApJ, 914, 25
Liu, J., Qiu, K., Wyrowski, F., et al. 2018, ApJ, 860, 106
Liu, J., Qiu, K., & Zhang, Q. 2022a, ApJ, 925, 30
Liu, J., Zhang, Q., & Qiu, K. 2022b, FrASS, 9, 943556
Liu, J., Zhang, Q., Qiu, K., et al. 2020, ApJ, 895, 142
Loughran, L., McBreen, B., Fazio, G. G., et al. 1986, ApJ, 303, 629
Maury, A. J., Girart, J. M., Zhang, Q., et al. 2018, MNRAS, 477, 2760
McBreen, B., Fazio, G. G., Stier, M., & Wright, E. L. 1979, ApJL, 232, L183
McKee, C. F., & Ostriker, E. C. 2007, ARA&A, 45, 565
McMullin, J. P., Waters, B., Schiebel, D., Young, W., & Golap, K. 2007, in
   ASP Conf. Ser. 376, Astronomical Data Analysis Software and, ed.
   R. A. Shaw, F. Hill, & D. J. Bell (San Francisco, CA: ASP), 127
Mouschovias, T. C. 1976a, ApJ, 206, 753
Mouschovias, T. C. 1976b, ApJ, 207, 141
Munoz, D. J., Mardones, D., Garay, G., et al. 2007, ApJ, 668, 906
Naghizadeh-Khouei, J., & Clarke, D. 1993, A&A, 274, 968
Palau, A., Zhang, Q., Girart, J. M., et al. 2021, ApJ, 912, 159
Pattle, K., & Fissel, L. 2019, FrASS, 6, 15
Pattle, K., Fissel, L., Tahani, M., Liu, T., & Ntormousi, E. 2022, arXiv:2203.
   11179
Persi, P., & Tapia, M. 2008, in Handbook of Star Forming Regions, Volume II,
  ed. B. Reipurth, Vol. 5 (San Francisco, CA: ASP), 456
Planck Collaboration, Abergel, A., Ade, P. A. R., et al. 2014, A&A, 571, A11
Planck Collaboration, Ade, P. A. R., Aghanim, N., et al. 2016, A&A,
   586, A138
Planck Collaboration, Akrami, Y., Ashdown, M., et al. 2020, A&A,
   641, A4
Qiu, K., Zhang, Q., Wu, J., & Chen, H.-R. 2009, ApJ, 696, 66
Remazeilles, M., Delabrouille, J., & Cardoso, J.-F. 2011, MNRAS, 418, 467
Rodriguez, L. F., Canto, J., & Moran, J. M. 1982, ApJ, 255, 103
Russeil, D., Zavagno, A., Adami, C., et al. 2012, A&A, 538, A142
Savage, B. D., & Jenkins, E. P. 1972, ApJ, 172, 491
Sanhueza, P., Girart, J. M., Padovani, M., et al. 2021, ApJL, 915, L10
Seifried, D., Walch, S., Weis, M., et al. 2020, MNRAS, 497, 4196
Skalidis, R., & Tassis, K. 2021, A&A, 647, A186
Soler, J. D., Hennebelle, P., Martin, P. G., et al. 2013, ApJ, 774, 128
Soler, J. D., Ade, P. A. R., Angile, F. E., et al. 2017, A&A, 603, A64
Stephens, I. W., Looney, L. W., Kwon, W., et al. 2013, ApJL, 769, L15
Tang, Y.-W., Koch, P. M., Peretto, N., et al. 2019, ApJ, 878, 10
Teague, R. 2019, RNAAS, 3, 74
Vaillancourt, J. E. 2006, PASP, 118, 1340
Ward-Thompson, D., Pattle, K., Bastien, P., et al. 2017, ApJ, 842, 66
Willis, S., Marengo, M., Allen, L., et al. 2013, ApJ, 778, 96
Wu, Y. W., Sato, M., Reid, M. J., et al. 2014, A&A, 566, A17
Yuen, K. H., & Lazarian, A. 2017a, ApJL, 837, L24
Yuen, K. H., & Lazarian, A. 2017b, arXiv:1703.03026
Zhang, Q., Qiu, K., Girart, J. M., et al. 2014, ApJ, 792, 116
```